# A Low Order Aerodynamic Model of Embedded Total Temperature Probes

Nicole Amanda Heersema

Thesis submitted to the faculty of the Virginia Polytechnic Institute and State University
in partial fulfillment of the requirements for the degree of

Master of Science
In
Aerospace Engineering

K. Todd Lowe, Chair
Lin Ma
Kevin Shinpaugh

9 October 2014
Blacksburg, VA

Keywords: aeroengine, total temperature sensors, embedded

**A Low Order Aerodynamic Model of Embedded Total Temperature Probes**

**Nicole Amanda Heersema**

# *ABSTRACT*

Measurement of the total conditions downstream of fans is of primary importance to aeroengine development. Historically, these measurements have been acquired with the use of traditional total condition probes mounted to the guidevanes or engine cowling; however, such a setup can have significant impact on the flow. Difficulties in obtaining direct measurements with traditional total conditions probes have led to the development of an embedded shielded probe. In order to support this development, a model was desired to be developed that accurately modelled the recovery using a low-order analysis that could be implemented quickly. The creation and validation of such a model is the primary focus of the present research. Of secondary interest is to prove the hypothesis that aerodynamics will dominate the recovery of such a sensor.

Based around the calculations for recovery used by Moffat, the model uses a linear vortex panel method to calculate the aerodynamics of the sensor. Higher order corrections were also suggested to improve the accuracy of the model. Several of these corrections, which take into account compressibility and variance of individual recovery factors, were included in the final model. Other corrections, such as improved paneling for the panel method and the inclusion of pitch angle have not been incorporated at this time but are part of an ongoing effort to improve and expand the capabilities of the model.

Model validation was performed in three steps, starting with comparing the calculations for the recovery without aerodynamics to values present in literature for traditional Shielded probes. The aerodynamics and the panel method used to generate them were validated separately using the widely available program Xfoil. Validation of the combined model could only be accomplished via experimental testing.

Several sensors, based on the predictions of the model, were 3D printed for use in experimental testing. Three key geometric parameters were identified and varied within the limits of interest to create the set of sensors tested. The purpose of this was two-fold. One: validate the model or identify key missing aerodynamic effects for inclusion. Two: prove the secondary hypothesis that aerodynamics will dominate the recovery. Testing was performed at a range of Mach numbers, yaw angles, and pitch angles commonly present in aeroengines.

The data collected for model validation were simultaneously used to prove the hypothesis that aerodynamic effects dominated the recovery. This hypothesis was concluded to be true for the range of parameters tested.

The model was determined to be valid for the range of parameters tested, although with the caveat that not all aerodynamic effects are fully accounted for and physical testing or CFD analysis is advised to verify results once design parameters have been narrowed down sufficiently. Further refinement of the experimental data and investigation of the aerodynamic effects are the subject of further study.

## *DEDICATION*

To my parents
and all of my part-time parents
for your love and support
and most especially,

To Ken “Daddy” Stiefel
My part-time Dad
Loved by so many and so much
You are missed

## *ACKNOWLEDGEMENTS*

Thanks are owed to the many people who supported this thesis, both financially and with words of encouragement:

My parents – for all of their love and support these many years

Dr. Lowe – for finding me a fun project to work on and for all of the suggestions and advice

Nick – for being my sanity when I had none left

Pratt and Whitney (particularly Justin): for sponsoring this research

Members of my committee: for their invaluable advice

AOE machine shop

Tyler & Donnie

Gracie & John

Friends & Family

And the many others who are not listed here. You know who you are.

You have my thanks.

# Table of Contents

ABSTRACT ..... ii
DEDICATION ..... iii
ACKNOWLEDGEMENTS ..... iii
NOMENCLATURE ..... vi
Table of Figures ..... viii
Chapter 1: Introduction ..... 1
1.1 Motivation for Embedded Total Temperature Sensors ..... 1
1.2 Literature Review ..... 3
1.2.1 Total Condition Probes ..... 3
1.2.2 Embedded Probes ..... 6
1.2.3 Analysis Methods ..... 7
1.3 Sensor Design ..... 9
1.3.1 Traditional Kiel Probe ..... 10
1.3.2 Embedded Shielded Sensor ..... 10
1.3.3 Sensor Geometry ..... 11
1.4 Organization of Thesis ..... 14
Chapter 2: Model Development ..... 15
2.1 Linear Vortex Panel Method ..... 16
2.1.1 Assumptions ..... 16
2.1.2 Paneling ..... 17
2.1.3 Vortex Strength ..... 17
2.1.4 Reversed Flow ..... 19
2.2 Recovery Ratio ..... 19
2.2.1 Concept of linearized temperature error ..... 20
2.2.2 Convective Error ..... 21
2.2.3 Conduction Error ..... 23
2.2.4 Radiative Error ..... 24
2.2.5 A Note on Recovery Factors ..... 25
2.3 Higher Order Corrections ..... 27
2.3.1 Aerodynamic Recovery Factors ..... 27
2.3.2 Karman-Tsien Compressibility Correction ..... 28

2.3.3 Paneling ..... 29
2.4 Validation of Components of the Model ..... 30
2.4.1 Validation of the Recovery Ratio Equations ..... 30
2.4.2 Validation of Panel Method ..... 31
Chapter 3: Validation Experiment Setup ..... 35
3.1.1 Facility ..... 35
3.1.2 Data Collection ..... 35
3.1.3 Data Processing ..... 38
Chapter 4: Experimental Validation Results ..... 40
4.1 Validation of Model ..... 40
4.1.1 Effect of Bleed Hole Diameter ..... 41
4.1.2 Effect of Bleed Hole Location ..... 43
4.1.3 Effect of Inlet Chamfer ..... 46
4.2 Pitch angle results ..... 47
4.3 Corrections ..... 48
4.4 A note on experimental repeatability ..... 49
Chapter 5: Model Predictions ..... 52
5.1.1 Effect of Bleed Hole Diameter ..... 52
5.1.2 Effect of Bleed Hole Location ..... 53
5.1.3 Effect of Inlet Chamfer ..... 55
5.1.4 Effects of Higher Order Corrections ..... 56
5.2 Optimal Design ..... 60
Chapter 6: Conclusions ..... 61
References ..... 63

# *NOMENCLATURE*

Symbol

| | |
|---|---|
| A1 | Flow area within stagnation tube, in2 |
| Ab | Total bleed area, in2 |
| Ac | Area available for convective heat transfer, in2 |
| AR | Area available for radiative heat transfer, in2 |
| Aw | Thermocouple wire frontal area, in2 |
| Aeff | Average effective flow area, in2 |
| Cd | Bleed discharge coefficient, dimensionless |
| Cp | Coefficient of pressure, dimensionless |
| Cp0 | Ideal coefficient of pressure, dimensionless |
| db | Bleed hole diameter, in |
| d1 | Inlet diameter, in |
| dw | Thermocouple wire diameter, in |
| hc | Convective heat transfer coefficient, $^{BTU}/_{Hr * ft^2 * °R}$ |
| kf | Thermal conductivity of air, $^{BTU}/_{Hr * ft * °R}$ |
| KR | Radiation form factor |
| ks | Thermal conductivity of thermocouple, $^{BTU}/_{Hr * ft * °R}$ |
| L | Length of thermocouple wire inside stagnation tube, in |
| M | Freestream Mach number, dimensionless |
| M1 | Inlet Mach number, dimensionless |
| Mb | Mach number at bleed holes, dimensionless |
| N | Number of bleed holes, dimensionless |
| Nu | Nusselt number, dimensionless |
| P0 | Freestream total pressure, psi |
| Pb | Pressure at bleed holes, psi |
| R | Recovery Ratio, dimensionless |
| Re | Reynolds number, dimensionless |
| rt, α | Convective recovery factor, dimensionless |

| | |
|---|---|
| rb, β | Conductive recovery factor, dimensionless |
| rs, κ | Radiative recovery factor, dimensionless |
| T0 | Freestream total temperature, °R |
| Tc | Conduction error component temperature, °R |
| Tmeasured, Tm | Measured plenum temperature, °R |
| Tsensor | Measured sensor temperature, °R |
| Tr | Radiation error component temperature, °R |
| Ts | Static temperature, °R |
| Tv | Convective error component temperature, °R |
| Tw | Wall temperature, °R |
| ΔT | Measured temperature difference (Plenum-Sensor), °R |
| ΔV | Measured voltage difference (Plenum-Sensor), Volts |
| (ΔT)v | Convective temperature error, °R |
| (ΔT)c | Conductive temperature error, °R |
| (ΔT)r | Radiative temperature error, °R |
| γ | Ratio of specific heats of air, dimensionless |

# *Table of Figures*

Figure 1.1 Basic schematic of total temperature sensor: an airfoil with an embedded flow channel. ..... 2
Figure 1.2. Depiction of stator blade with embedded Kiel probe from patent [1]. ..... 7
Figure 1.3. A cross section of the sensor showing the interior flow channel and relevant geometry. ..... 13
Figure 2.1. Overview of analysis method. ..... 15
Figure 2.2. Profile of actual sensor (top) vs modelled sensor (bottom) with evenly spaced panels and control points. Increasing the number of panels improves the accuracy of the approximation. ..... 16
Figure 2.3. Comparison of the recovery correction factor equations to the data obtained by Willbanks [34] ..... 31
Figure 2.4 Pressure distribution linear vortex panel method (left) vs xfoil (right) for select parameter set at three yaw angles. ..... 33
Figure 2.5 Lift coefficient vs yaw angle for linear vortex panel method and xfoil. ..... 34
Figure 3.1 Overview diagram of the supersonic hot jet facility detailing the flow conditioning used ..... 35
Figure 3.2. Overview of the experimental setup depicting the type and approximate location of all sensors used ..... 37
Figure 4.1. Comparison between model prediction and experimental data vs yaw angle for bleed hole diameter. ..... 42
Figure 4.2. Comparison between model prediction and experimental data versus Mach number for bleed hole diameter ..... 43
Figure 4.3. Comparison of model prediction to experimental data versus yaw angle for bleed hole location. ..... 44
Figure 4.4. Comparison of model prediction to experimental data versus Mach number for bleed hole location ..... 45
Figure 4.5. Comparison of model predictions to experimental data versus yaw angle for inlet chamfer ..... 46
Figure 4.6. Repeatability of select sensors for Mach number tests. A clear correlation exists between certain geometric parameters and the repeatability. ..... 50
Figure 5.1. The effect of bleed hole diameter on the yaw angle recovery ratio, as predicted by the model ..... 52
Figure 5.2. The effect of bleed hole diameter on the Mach number recovery ratio, as predicted by the model ..... 53
Figure 5.3. The effect of bleed hole location on the yaw angle recovery ratio, as predicted by the model ..... 54
Figure 5.4. The effect of bleed hole location on the Mach number recovery ratio, as predicted by the model ..... 54
Figure 5.5. The effect of inlet chamfer on the yaw angle recovery ratio, as predicted by the model. ..... 56
Figure 5.6. Effect of linearly varying recovery factors on the yaw characteristics for bleed hole diameter ..... 57

Figure 5.7. Effect of linearly varying recovery factors on the yaw characteristics for bleed hole location. ..... 58
Figure 5.8. Effect of linearly varying recovery factors on the yaw characteristics for inlet chamfer. ..... 59
Figure 5.9. Effect of Karmen-Tsien compressibility correction at high Mach number..... 59

# *Table of Tables*

Table 1.1 Summary of Winternitz's yaw range results. Select data of interest reproduced from Table 1 in Winternitz. ..... 6
Table 2.1 Complex Velocity of flow components ..... 18
Table 4.1. Pitch angle recovery results compared to geometric parameters. ..... 47

# Chapter 1: Introduction

## *1.1 Motivation for Embedded Total Temperature Sensors*

In the world of aeroengine development, there is a driving need to fully understand the temperature profile in the fan section of the engine. High fidelity interstage total pressure and temperature measurements are the standard means for measuring performance of turbomachines. Although much effort has been expended to improve such measurements over the past 90 years, the high performance of contemporary engine technology and the great influence that small incremental differences have on performance gains have created a need for innovative sensor concepts.

A design has been suggested that would embed traditional temperature sensors into blade-like struts in order to take direct measurements. In such a design, a fluid channel would be integrated into the strut to act as a shield for the probe. In traditional shielded instruments, the shield acts to deflect the stream onto the axis of the probe allowing accurate measurements at a wider range of flow angles. This would allow for high accuracy at the relatively high flow angles experienced by fan blades. Since the principle ideology of shielded instruments is to make use of the conservation of total conditions along a streamline in loss-free flow, such instruments are designed to have relatively low impact on the flow.

For this application, a high priority is placed on designing a sensor with low variability in yaw angle and Mach number, and with a high tolerance for slight variations in machining. In order to improve engine efficiency, new fan blades are being designed with twist, causing the fan blade to experience different flow angles along its length. A sensor designed to be placed at discrete intervals along the length of a fan blade would need to be insensitive to these changes in flow angle. Mach number also can vary considerably along the length of a fan blade, with the tip of the fan blade often being

the location of highest Mach number. The sensor must be designed such that changes in Mach number on the order usually seen in aeroengines will have only a minimal effect on sensor performance. A high tolerance is also required for slight variations in machining. The sensor must be designed such that a small variation in the geometry of the sensor or flow channel will have minimal impact on the performance of the sensor.

As the presence of the sensor alters the flow one is trying to measure, it is desired to ensure that the impact on the flow is minimal. Therefore, an understanding of how the presence of the sensor alters the aerodynamics of the fan path is highly important. While such an analysis commonly falls in the realm of Computational Fluid Dynamics (CFD), such an analysis is often unsuitable for initial design. CFD analyses tend to be very costly and take a lot of time and computational power to set up and run a single analysis. For an initial design such as this, where many design variations may be considered, a full CFD analysis would take far too much time. Once a design is closer to finalization, a thorough CFD analysis may be required to create a more complete picture of the flow conditions. For initial design, however, a lower order model that is quicker to implement is more suitable in many cases. It was determined that a need exists for a simplified model as a first step towards direct measurement of flow properties in the fan section of an aeroengine. This model, while low-order, would need to have high accuracy and be quick to implement. The model is discussed further in Chapters 2 and 3.

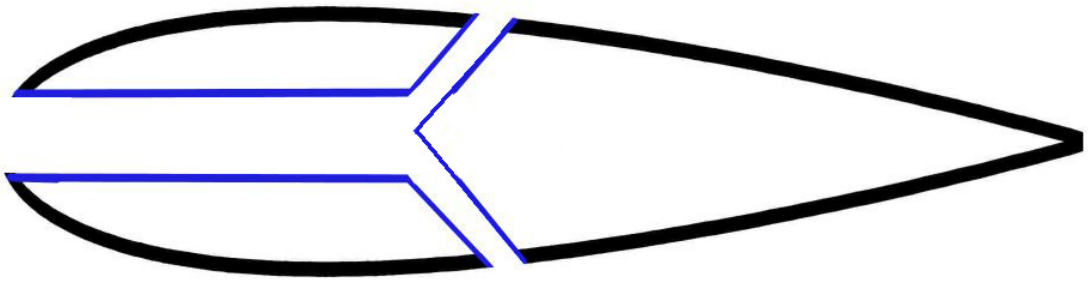

**Figure 1.1 Basic schematic of total temperature sensor: an airfoil with an embedded flow channel**.

Although a basic design, consisting of an airfoil with an embedded flow channel such as shown above, has already been developed for this application, an understanding of the design sensitivity of the geometry has been deemed necessary. To that end, several variations of the design will be studied in which certain geometric parameters are varied. The primary geometric parameters that govern the flow conditions through traditional shielded instruments are inlet geometry, bleed hole location, and inlet to bleed hole area ratio. [31] For this analysis, the inlet area and number of bleed holes are held constant so the inlet to bleed hole area ratio may be quantified in terms of the bleed hole diameter. For this analysis, three different inlet geometries were considered. Likewise, three different bleed hole diameters were considered within the limits of traditional shielded instruments. Two bleed hole locations were considered based on the aerodynamics of the sensor.

A secondary purpose of this study is to test the hypothesis that aerodynamics of the sensor will dominate the recovery of the sensor. This will be accomplished by comparing the recovery of the sensors based on their geometric parameters to the expected differences in aerodynamics for the different geometric parameters. If the changes in recovery match the expected changes based on the aerodynamics, then this hypothesis will be considered correct.

## *1.2 Literature Review*

An extensive review of available literature was conducted to determine the state of the art technology and analysis methods of embedded total condition probes.

### 1.2.1 Total Condition Probes

Aeroengine compressor tests often utilize shielded probes mounted at the leading edge of a stator to measure the span-wise distribution of total pressure and total temperature. Copenhaver et al. [7] describe one such case in which Shielded probes are

mounted on the leading edge of stator blades to try to understand the influence of design factors on rotating stall recoverability of a high-speed multistage compressor. Copenhaver et al. needed to measure total pressure and temperature at different locations for different design speeds and used Shielded probes due to their insensitivity to flow direction.

In Xiang et al. [37] an analysis is performed on the effect of leading-edge mounted Shielded probes on the performance of an axial compressor. The authors make use of a full CFD analysis coupled with experimental testing [37] to investigate the influence these probes have on the compressor performance at design and off-design conditions. It was determined that the presence of these probes results in a 1.1% decrease in peak efficiency. The probes were also shown to induce streamwise vortices on both sides of the stator blade, which have greater effects when the flow angle is greater.

In 1956 Gracey [11] conducted a study on total pressure tubes at high angles of attack. This study compared the insensitivity range of shielded and non-shielded tubes. Various configurations of the non-shielded tubes were investigated, as were vented and non-vented shielded tubes. In all, 54 different tubes were tested. The insensitivity range was used as a criterion for comparing performance and is defined as the range of flow angle over which the tubes remain within 1% of true value. The effect each of the various design parameters had on the performance was determined by directly comparing the insensitivity ranges. Several of the design parameters relevant to this analysis are: the effect of venting on Kiel-type shielded tubes, the effect of varying location of the probe with respect to the leading edge of the shield, the effect of Mach number, and the effect of inlet chamfer. As originally designed, the Kiel probes had no venting, and were more limited in their use. The addition of venting allowed for greater range of use as well as a greatly increased insensitivity range. The addition of a total vent area equal to half the frontal area of the shield increased the insensitivity range by almost 15°. A further increase in vent area did not produce a significant increase in insensitivity range.

This insensitivity range was determined to decrease with increasing Mach number. More important for this analysis, as it is a design variable not well accounted for, is the effect of varying probe position with respect to the leading edge of the shield. It was determined that as long as the probe is within ½ inlet diameter of the leading edge of the shield, its exact position has no significant effect on the performance. The effect of the inlet chamfer angle is also important as it helped guide the choice of inlet chamfer angle used in this analysis. Gracey determined that an increase in internal chamfer angle from 25 degrees to 120 degrees will increase the insensitivity range by 20 degrees at a Mach number of 0.26.

In a study by Marowski et al. [19] a smaller version of a traditional Kiel sensor was suggested which would be significantly more useful for measurements of fan blades. The size of the original Kiel probe prevents its use in flow surveys in turbomachinery. It was therefore deemed desirable to design a smaller version with the same characteristics and performance as the original, which Moffat et al. were successful in doing. However, in that study only the exterior dimensions were provided so Winternitz [36] performed an analysis to determine the optimal interior dimensions. There was also a desire to create a simplified version for easier manufacturing as it had been determined that the quality of workmanship had a fairly significant effect on the probe characteristics. In the original Kiel design, an improperly centered sting would result in an asymmetry of characteristics and any bend in the tube could easily result in a near blockage. Several different configurations were tested and the results summarized in Table 2.1.

**Table 1.1 Summary of Winternitz's yaw range results. Select data of interest reproduced from Table 1 in Winternitz.**

| | Shield Length (in) | Shield Diameter, i.d./o.d. (in) | Setup | Sting/Cylinder Diameter, i.d./o.d. (in) | 1% error limit AoA range, ° |
|---|---|---|---|---|---|
| Probe 1 | 0.3 | 0.072/0.100 | Sting | 0.010/0.024 | ±45 |
| Probe 2 | 0.3 | 0.072/0.100 | Sting | 0.038/0.056 | ±23 |
| Probe 3 | 0.3 | 0.072/0.100 | Sting | 0.025/0.030 | ±40 |
| Probe 4 | 0.3 | 0.080/0.125 | Sting | 0.026/0.036 | ±45 |
| Probe 5 | 0.3 | 0.082/0.114 | Cylinder | 0.012/0.022 | ±15 |
| Probe 6 | 0.3 | 0.082/0.114 | Cylinder | 0.024/0.036 | ±29 |
| Probe 7 | 0.3 | 0.082/0.114 | Cylinder | 0.026/0.036 | ±28 |

The cylindrical design offers an ease of manufacturing and a faster response time, but has a limited useful range. Based on the results of Winternitz's study, it was determined that a sting-type design is the best choice for this analysis.

In addition to these studies consulted in detail, there are number of other notable references on the topic [3, 5, 6, 8, 12, 14, 15, 17, 18, 22, 23, 26, 27, 30, 32, 33].

### 1.2.2 Embedded Probes

Gander et al. [10] present an alternative to traditional pressure instruments for experimental investigation of turbine aerodynamics. Several different commonly used electrical pressure sensors are referenced, each with limitations that restrict their use in turbomachinery applications. Compared with these, the micromachined Fabry-Perot optical-fiber pressure sensor, presented by Gander et al. [10], promises potential advantages, such as smaller size and lower cost. Another advantage, which is of particular relevance to this study, is the ability to embed the pressure sensor directly into the test article due to the small size. The sensors were embedded flush with the trailing edge, maintaining the original shape of the nozzle guide vane.

In the 1960s, a patent was issued for a stator blade with an embedded Kiel probe [1]. This patent, which provides no dimensions or testing data, describes the process for fabricating a stator blade with a Kiel embedded in the leading edge, as shown in Figure 1.2. However, it is also evident from the same figure that the design requires that the profile of the vane be deformed in order to accommodate the Kiel shroud.

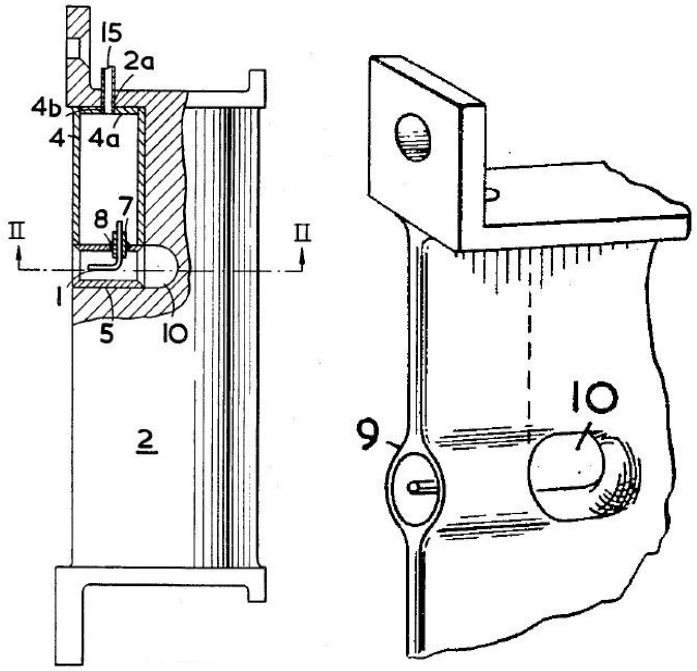


**Figure 1.2. Depiction of stator blade with embedded Kiel probe from Annear, J.D., White, H., Holt, S., Power Jets Limited, London, England, U.S. Patent Application for a "Stator Blade Mounting of Condition Sensing Elements in Fluid Flow Machines," no. 295021, filed 9 July 1954. Used under Fair Use, 2014.**

A search of available literature did not yield any references to this design ever being used. Due to the deformation of the original profile due to the embedded Kiel probe, this design was not used in this study.

## 1.2.3 Analysis Methods

Several different analysis methods were considered, based on the analysis methods used in similar studies.

Rossow [24] makes use of a panel method to determine the optimal geometric parameters for a probe used in highly turbulent flows. The panel method used in that analysis was developed by Ashby et al. [2]. The potential flow code described by Ashby is a 3D low order panel code which includes advanced features such as internal flow modeling, simple jet wake modeling, and a time-stepping wake model. In this code, the 3D surface is divided into quadrilateral panels over which a constant-strength source and doublet are distributed. The source values are determined using the Neumann boundary condition which states that the velocity normal to the control point of the panel must be zero. A fast iterative matrix solver is used to perform the calculations quickly and with a minimal amount of memory required. Rossow primarily made use of the jet wake modeling to model crossflow, but for this analysis the internal flow modeling is of much greater interest. Flow through ducts or channels can be modelled using the internal flow model. The internal flow geometry is modeled as a closed box with each panel normal vector pointing towards the interior of the box. Inflow and outflow are prescribed as normal velocities on groups of panels and must satisfy the continuity equation. The internal flow is solved in a similar manner to the external flow, except that the doublet value for one panel must be arbitrarily specified to avoid a singular matrix. Once the matrix is solved, the correct source value, which satisfies the Neumann condition, is substituted for the arbitrary one. Higher accuracy can be achieved using a far field approximation, but at the cost of increased computation time.

Willcox [35] describes an alternate method to create a low-order high-fidelity aerodynamic model using a reduction of order technique. Simplified aerodynamic models already exist but are severely limited in scope and range of validity making them unsuitable for most complex flows, even at the design phase. Although a full CFD analysis is too time consuming and computationally expensive to use at the design phase, it is often the only way to fully capture the complex aerodynamics experienced inside an aeroengine. Applying a reduction of order technique allows the high fidelity of

the CFD model to be translated to a lower order model which is more computationally efficient and practical to implement within a design framework. High fidelity system dynamics can be captured with just a few states if the basis is chosen appropriately. Several of the reduction methods discussed in other papers are considered by Willcox for application to turbomachinery design. One possible method for a basis is computation of the eigenmodes of the system. This approach has been used before for flow around an isolated airfoil using Euler and Navier-Stokes equations [35] and for certain aspects of turbomachinery [35], however, typical problem sizes are much too large for the level of computational efficiency desired. Proper orthogonal decomposition can also be used to compute the basis using a set of instantaneous flow solutions obtained from CFD. This is often the most efficient method of capturing the dominant components of an infinite-dimensional process with a finite number of 'modes', often requiring surprisingly few modes. An Arnoldi based method was also considered using the Arnoldi algorithm to generate the basis vectors, which Willcox then applied to turbomachinery using an exploitation of the linearity of the governing equations. This approach proved to be valid over the range of parameters tested and very efficient. While Willcox focused on applying this method to equations governing aeroelastic response, a similar approach could be used for a wide range of aerodynamic applications, including the one discussed in this thesis.

## *1.3 Sensor Design*

This study is focused around the development and testing of a total temperature sensor. However, future work will include the expansion of the design to incorporate total pressure measurements as well. While the motivation for pressure and temperature sensors is slightly different, very similar designs can be used, reducing the amount of additional design and testing needed. This section presents a short synopsis of the history of the design of total condition sensors. Although the motivation is different for temperature and pressure sensors, the history follows similar paths. As the history of

total pressure sensors is considerably more interesting and better known, it is presented here in place of the history of total temperature sensors.

Historically, pressure measurements are often performed using a Pitot tube, which was invented in the early 18$^{th}$ century. Commonly used to determine the airspeed of an aircraft by coupling it with a static source and using Bernoulli's equation, the Pitot tube works by bringing the fluid inside the tube to rest in order to measure the total pressure. The primary disadvantage to the Pitot tube is that it is extremely sensitive to variations in yaw. This prevents it from being used in any situation where the angle of the flow is unknown, imprecise, or variable. For this analysis, measurements were needed at several different yaw angles, precluding the use of a traditional pitot tube.

### 1.3.1 Traditional Kiel Probe

Kiel probes were designed in 1935 to solve the problem of yaw sensitivity in Pitot probes. Similar in function, the Kiel probe is very similar to the Pitot probe except that it has a 'shield' or 'shroud' around the inlet. Kiel determined that housing the Pitot tube in a shroud allowed for a high accuracy at a much greater range of yaw. In fact, this one small alteration expanded the insensitivity yaw range to approximately ±45° [16]. The insensitivity yaw range is the range of yaw angles over which the error is less than 1% of the true measurement. At Mach numbers higher than Mach 0.3, this yaw range is slightly decreased.

### 1.3.2 Embedded Shielded Sensor

While traditional shielded probes are very useful in a wide range of applications, and have been used in turbomachinery applications, it was determined in Xiang [37] that the common method of mounting Kiel probes to the leading edge of the test article was detrimental to the flow that was being measured. The aerodynamics of the cylindrical shape of the shielded probe could easily result in streamwise vortices. A new method of attaching the probes to the test articles was required which would improve the aerodynamics and limit the effect on the flow to be measured. The idea was proposed

to embed the probe into the test article itself, making use of the airfoil shape to form the shield that is inherent in the shielded probe design. This proposed method would allow for measurements to be taken without significantly impacting the flow being measured.

For the particular application discussed here, an embedded shielded probe was thought to offer the best performance given the limitations. In order to embed the shielded probe into the profile, a flow channel was integrated into the profile to form the 'shroud' of the probe. Due to the desired use of this sensor, certain limitations were imposed on the design. These limitations, which mainly affected the profile of the sensor, were primarily driven by the need to have room for the measurement package without compromising structural integrity. The details of how the sensor profile was determined are not pertinent to this analysis. Once the basic profile of the sensor was determined, select geometric parameters were varied to determine the optimal design for the embedded flow channel.

### 1.3.3 Sensor Geometry

In order to determine the optimal sensor design, three geometric parameters were varied: inlet geometry, bleed hole diameter, and bleed hole location. The geometry of the flow channel also influences the performance of the sensor and is discussed below.

#### *1.3.3.1 Inlet Geometry*

As established by Gracey [11], a large internal chamfer angle is beneficial in expanding the insensitivity range of a Shielded probe. Based on this study and accounting for ease of fabrication, a 45° internal chamfer was chosen for the design. The other parameter needed to fully define the inlet geometry is the location of the inlet with respect to the unaltered profile. This parameter is defined as the distance between the unaltered leading edge and the opening in the altered profile along the chord as a percentage of the inlet diameter. Figure 1.3 shows the effect of inlet geometry on the profile of the sensor, which is an increase in the capture area. For this analysis two values of this

parameter were chosen. They will be referred to as medium chamfer and large chamfer.

However, the complexity of the inlet chamfer made modelling of it difficult, so the inlet was modelled as a flat plate with a diameter equal to the total diameter of the chamfered inlet. In order to fully understand the effects of the chamfer to better incorporate them into the model, an additional sensor design with no chamfer was included in this analysis. It will be referred to as zero or small chamfer.

#### *1.3.3.2 Bleed Hole Diameter*

Venting of shielded sensors proved to be a significant factor in the performance of the sensors; however, very little study has been conducted on the optimal size and location of the vent, or bleed, holes. Gracey [11] determined that a vent area of half of the inlet area provided a significant increase in insensitivity range, but also that any further increase had much less effect. Since a bleed hole area ratio of 50% has already been shown to be an effective upper limit, it was desired to investigate if the insensitivity range increased linearly up to that point or if there was an effective lower limit. To that effect, three bleed hole sizes were chosen so as to attain three total bleed hole area ratios evenly spaced with none being greater than 50%. These bleed hole sizes are referred to by their diameters as: small diameter, medium diameter, and large diameter.

#### *1.3.3.3 Bleed Hole Location*

While little study had been performed on the effect of bleed hole to inlet area ratio, no studies have been found that address the effect of bleed hole location. It is commonly agreed that the bleed holes must be located downstream of the instrument in order to get an accurate measurement of the flow property desired; however, it is unknown if the exact location relative to the instrument matters. Given that the profile of a traditional cylindrical Shielded probe does not change in the streamwise direction, there little reason to suspect that this location matters, so long as it is sufficiently far downstream. For an embedded Shielded probe, however, the profile does change in the

streamwise direction, impacting the flow and creating a significant pressure difference between different locations along the sensor. For this reason, the location of the bleed holes is believed to have a much greater effect. It is even possible to experience reversed flow through the flow channel if the bleed hole location is not chosen wisely. To study the potential effects of bleed hole location, two locations were chosen: one near the point of maximum pressure and one just forward of the separation point at zero degrees yaw. These locations will be referred to as fore or forward location and aft location, respectively.

### *1.3.3.4 Geometry of Flow Channel*

The internal geometry of the sensor has been much more extensively studied for traditional Shielded probes, most notably by Winternitz [36] in his efforts to create a simplified Shielded probe for easier manufacturing. Given his results, a fairly simple geometry was chosen for the flow channel. Figure 1.3 shows the geometry of the internal flow channel.

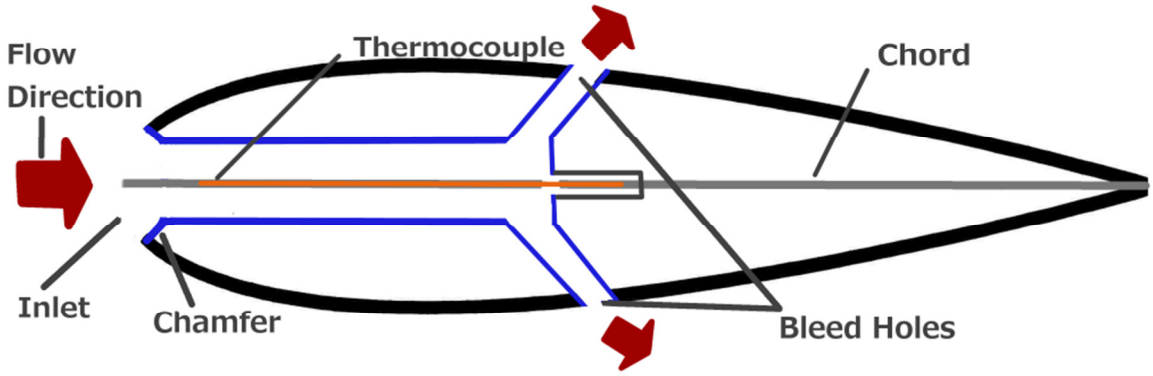


**Figure 1.3. A cross section of the sensor showing the interior flow channel and relevant geometry.**

The flow channel is a simple cylinder with a diameter matching the chosen inlet diameter. At the end of this cylinder is a small channel which is used to insert the thermocouple. Once the thermocouple has been inserted, the channel is sealed to prevent leakage of the air from the flow channel.

## *1.4 Organization of Thesis*

This thesis is organized into six chapters, including this one. Chapter 2 describes the development of the low-order analytical model. Chapter 3 details the experimental setup used for validation. Model validation in Chapter 4 and Chapter 5 contains model predictions. Chapter 6 provides the conclusions gathered from the study. References used in this thesis can be found immediately following Chapter 6.

# Chapter 2: Model Development

In order to accurately model the flow through the sensor a full CFD analysis would be required. Given the high computational and time costs of such an approach, a lower order model was developed. This model would be able to predict the performance of a particular design to a desired degree of accuracy at a fraction of the time required for a CFD analysis. Due to the complex geometry of the interior of the sensor, a method was developed to determine the flow through the sensor based on certain characteristics of the flow around the sensor. In this method, a linear vortex panel method was used to calculate pressure coefficients at desired locations on the exterior of the sensor. From those, desired parameters could be calculated using simple aerodynamic relations. Figure 2.1 provides an overview of this procedure.

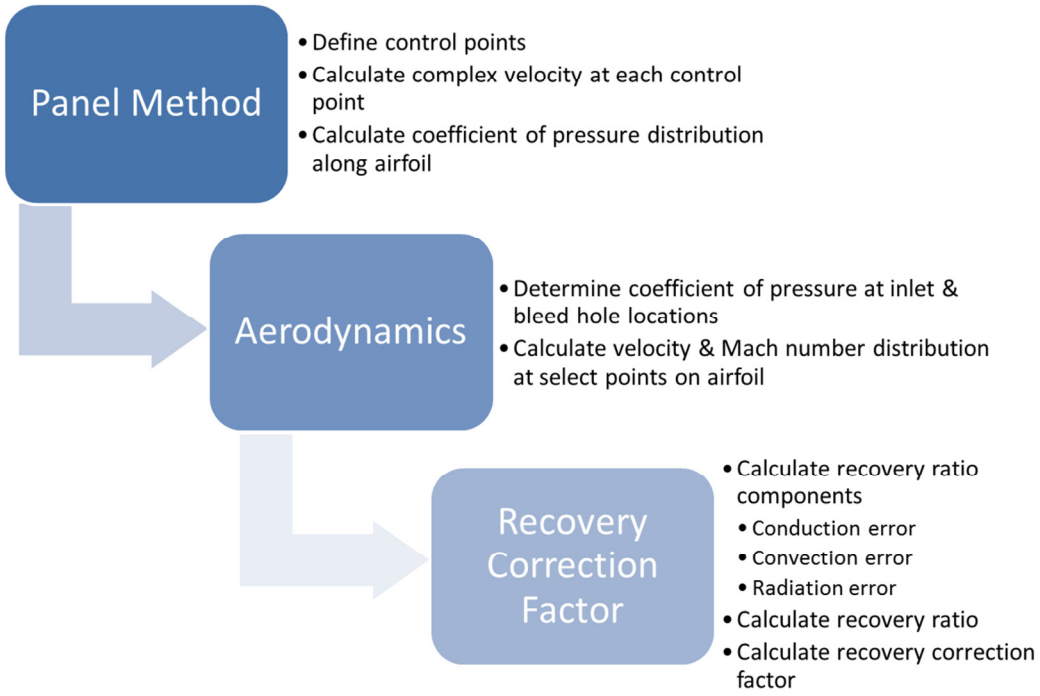


**Figure 2.1. Overview of analysis method.**

## *2.1 Linear Vortex Panel Method*

The linear vortex panel method was used to determine the pressure and velocity along the exterior of the airfoil. Since the complexity of the interior flow channel prevents direct calculation of the interior flow, certain assumptions were made regarding the interaction of the interior and exterior flows. Flow around the exterior of the sensor is calculated assuming a solid cross section with no interior flow channel. While this approach may not capture all of the intricacies of the flow, such as the effect of turning, it is simpler to implement and reduces computational time.

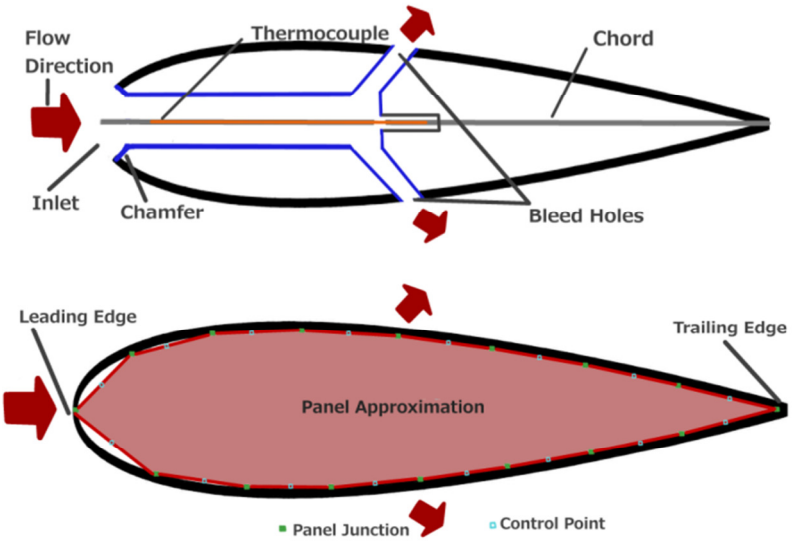


**Figure 2.2. Profile of actual sensor (top) vs modelled sensor (bottom) with evenly spaced panels and control points. Increasing the number of panels improves the accuracy of the approximation.**

### 2.1.1 Assumptions

At the inlet it is assumed that the pressure of the flow entering the channel is the same as the stagnation pressure of the sensor without the interior flow channel. Since shielded probes are designed to measure stagnation conditions, this is an acceptable

assumption to make for a low order analysis. Furthermore, it is assumed that the pressures of the exterior flow at the inlet and outlet of the channel drive the flow through the channel. Therefore, at the outlet of the flow, the pressure of the flow exiting the channel is assumed to match the pressure of the flow on the exterior of the sensor at that location. These assumptions allow the flow through the channel to be modelled based on the flow around the sensor.

### 2.1.2 Paneling

Panel methods model a given body as a series of straight panels which approximate the shape as accurately as desired, as in Figure 2.2. These panels connect a series of designated points. These points may be equally spaced around the object or concentrated in areas of particular interest, such as the leading and trailing edges of an airfoil. Each panel has a centrally located control point used in velocity calculations. Figure 2.2 shows an airfoil with equally spaced panels, such as is used in this analysis. It is important to note that a trade-off exists between the number of panels and the computational cost as the number of panels equals the number of equations that must be solved simultaneously.

### 2.1.3 Vortex Strength

The linear vortex panel method assumes linearly varying vortex strength along each panel with the strength remaining constant across panel joints. These panel strengths are unknown and their solution is the primary purpose of this technique. Calculations involving flow velocities are expressed in the complex plane.

The form of W(z) for various common shapes is well understood and is given in Table 2.1 for several flow components used in this analysis. Superposition allows for a real flow to be modeled as the simple sum of its components.

**Table 2.1 Complex Velocity of flow components**

| Flow Component | Complex Velocity, W(z) |
|---|---|
| Uniform flow of $V_\infty$ at angle $\alpha$ | $V_\infty e^{-i\alpha}$ |
| Vortex at $z_1$ producing circulation $\Gamma$ | $\frac{-i\Gamma}{2\pi(z-z_1)}$ |

For the linear vortex panel method, the velocity over each panel is defined only at the control point for that panel and is modeled as:

$$W(z) = V_\infty e^{-i\alpha} - \frac{i}{2\pi}\int_{panel}^{\cdot} \frac{\gamma(s)ds}{(z-z_1(s))} \quad (1)$$

where W is the complex velocity of the flow around the airfoil, $V_\infty$ is the freestream velocity, α is the angle of the flow, and γ is the vortex strength per unit length.

### *2.1.3.1 Coefficient of Pressure*

Certain conditions must be imposed to produce a realistic flow. At the mid-point of each panel the velocity perpendicular to that panel is calculated and set to zero to enforce the condition that no flow is permitted through the panel.

$$Im\left\{W(z)\frac{dz}{d\zeta}\right\} = 0 \quad (2)$$

The Kutta condition, which states that the rear stagnation point must be at the trailing edge, is also enforced. Solving the simultaneous equations allows certain flow parameters to be evaluated. The coefficient of pressure, $C_p$, is calculated using Bernoulli's equation for inviscid incompressible flow:

$$C_p = 1 - \frac{|W(z)^2|}{V_\infty^2} = 1 - \frac{|W(\zeta)^2|\left|\frac{d\zeta}{dz}\right|^2}{V_\infty^2} \quad (3)$$

The pressure at the inlet and the bleed holes are calculated from the pressure coefficients and the freestream conditions. Since there are multiple bleed holes at different points in the flow, it is assumed that the bleed hole with the greatest pressure drives the flow. The Mach number at the bleed hole is then calculated as:

$$M_b = \sqrt{\frac{2}{\gamma-1}\left[\left(\frac{P_0}{P_b}\right)^{(\gamma-1)/\gamma} - 1\right]} \quad (4)$$

where Mb is the Mach number at the bleed holes. Once the pressure and Mach number for the sensor inlet and bleed holes have been calculated, the values are used in the Recovery Ratio calculations.

### 2.1.4 Reversed Flow

Physically, it is possible for there to be fluid flowing backward through the channel in a condition known as reverse flow. Such a condition occurs when the pressure at the bleed hole is greater than the pressure at the inlet, driving flow backwards through the channel. Although such conditions would still produce flow across the sensor embedded in the channel, producing a value for the Recovery Ratio, this would not be accurately reflective of the true flow. As such, in the model all reverse flow is assumed to yield a 'no flow' condition, and an error is produced if the pressure ratio $\left(P_0/P_b\right)$ is less than 1.

## *2.2 Recovery Ratio*

The accuracy of the total temperature measurement is characterized using the recovery ratio, a measure of how much of the temperature of the flow is 'recovered' by the

sensor. The recovery ratio equations are a zero-dimensional set of quasi-empirical aerothermodynamics equations intended to model axisymmetric sensors. The recovery ratio of the sensor is based upon the combined temperature error of the sensor, $(\Delta T)_p$ , and is given as:

$$R = \frac{T_p}{T_T} = 1 - \frac{(\Delta T)_p}{T_T} \tag{5}$$

In a significant portion of literature, the recovery is reported in terms of the recovery correction factor instead of the recovery ratio. The two are related as:

$$\Delta = 1 - R \tag{6}$$

where Δ is the recovery correction factor. In keeping with literature, the recovery correction factor will be used to present results.

### 2.2.1 Concept of linearized temperature error

If the assumption is made that environmental effects, which primarily effect the conduction and radiation errors, are small, which is a valid assumption as the goal of sensor design is to minimize impact on the flow, then the total error may be assumed to be a linear combination of the individual errors. Under this assumption the presence of one effect has no influence on the values of the other effects. The combined temperature error of the sensor may then be calculated as:

$$(\Delta T)_p = (\Delta T)_v + (\Delta T)_c + (\Delta T)_r \tag{7}$$

where $(\Delta T)_v$, $(\Delta T)_c$, and $(\Delta T)_r$ are the temperature errors due to convection, conduction, and radiation, respectively. This equation is substituted into the equation for recovery ratio to yield:

$$\frac{T_p}{T_0} = 1 - \frac{(\Delta T)_v}{T_0} - \frac{(\Delta T)_c}{T_0} - \frac{(\Delta T)_r}{T_0} \tag{8}$$

For algebraic convenience, the three error components may be defined in terms of their respective component temperature ratio as:

$$\begin{aligned} \frac{T_v}{T_0} &= 1 - \frac{(\Delta T)_v}{T_0} \\ \frac{T_c}{T_0} &= 1 - \frac{(\Delta T)_c}{T_0} \\ \frac{T_r}{T_0} &= 1 - \frac{(\Delta T)_r}{T_0} \end{aligned} \tag{10}$$

which yields an equation for the recovery ratio in terms of the component temperature ratios:

$$R = \frac{T_p}{T_0} = \frac{T_v}{T_0} + \frac{T_c}{T_0} + \frac{T_r}{T_0} - 2 \tag{11}$$

Recovery models have been derived by several authors [20, 21, 25, 28, 29]. Due to the completeness and good performance, the model of Moffat [21] is chosen for replication

### 2.2.2 Convective Error

In high speed, low temperature flow, the convective term tends to dominate. The derivation of the convective error component begins with the enthalpy equation for high speed flow as presented in Moffat [21]:

$$T_0 - T_s = (1 - \alpha)\frac{V^2}{2c_p} \tag{12}$$

The convective error component may then be calculated from freestream conditions and the aerodynamic recovery factor as:

$$1 - \frac{T_v}{T_0} = \frac{(1-\alpha)\frac{(\gamma-1)}{2}M_1^2}{1+\frac{(\gamma-1)}{2}M_1^2} \quad (13)$$

where $\gamma$ is the freestream ratio of specific heats, $\alpha$ is the aerodynamic recovery factor of the thermocouple, and $M_1$ is the inlet Mach. A baseline value of 0.85 was assumed for α based on the literature [9]. For a traditional Shielded probe, the inlet Mach would be calculated as:

$$M_1 = C_d M \left(\frac{1}{A_{eff}/A_b}\right)\left[1 + \frac{\gamma-1}{2}M^2\right]^{-3} \quad (14)$$

where $C_d$ is the discharge coefficient which is the ratio of the mass flow on the interior of the airfoil to the mass flow of the freestream[13]. The sensor's effective flow area, $A_{eff}/A_b$, is calculated from the stagnation tube's inlet area and the thermocouple's frontal blockage area as:

$$\frac{A_{eff}}{A_b} = \frac{1}{N}\left[\left(\frac{d_1}{d_b}\right)^2 - \left(\frac{1}{2} + \frac{2\left(\frac{s}{d_w}+1\right)}{\pi}\left(\frac{d_w}{d_b}\right)^2\right)\right] \text{[31]} \quad (15)$$

where $N$ is the number of bleed holes, $d_1$ is the inlet diameter, $d_b$ is the diameter of the bleed holes, $d_w$ is the diameter of the thermocouple wire, and $s$ is the spacing of the thermocouple wire. The frontal blockage area of the thermocouple is calculated from the thermocouple geometry as:

$$A_w = \frac{\pi}{4}d_w^2 + d_w^2 + sd_w \text{ [31]} \quad (16)$$

The equation for inlet Mach number assumes stagnation conditions within the stagnation tube and freestream static conditions in the bleed tubes. Since the embedded probe has different aerodynamics, the inlet Mach number is calculated from the compressible area-Mach number relation as:

$$\frac{A_1}{A_b} = \frac{M_b}{M_1}\left[\frac{\left(\frac{2}{\gamma+1}\right)\left(1+\frac{\gamma-1}{2}M_1^2\right)}{\left(\frac{2}{\gamma+1}\right)\left(1+\frac{\gamma-1}{2}M_b^2\right)}\right]^{\frac{\gamma+1}{2(\gamma-1)}} \quad (17)$$

where the area ratio $A_1/A_b$ is known and the Mach number at the bleed hole, $M_b$, is calculated from the pressure coefficient determined by the linear vortex panel method (Eqn. 4).

### 2.2.3 Conduction Error

For hot flows, the conduction term tends to dominate, particularly for metal sensors. It is important to note that in the current validation experiment using plastic probes, the conduction term is minimal due to insulating effects of the probe isolating the thermocouple wires.

The conductive error component may be calculated from freestream conditions, geometry, and the aerodynamic recovery factor as presented in Moffat [21]:

$$T_0 - T_c = 1 - \frac{T_c}{T_0} = \frac{T_0 - T_M}{\cosh L\sqrt{{4h_c}/{d_w k_s}}} \quad (17)$$

where L is the thermocouple length, $d_w$ is the diameter of the thermocouple, $k_s$ is the coefficient of thermal conductivity of the thermocouple [W/(m∗ K)],$h_c$ is the convective heat transfer coefficient [W/( $m^2$∗K)],], and:

$$T_0 - T_M = \frac{(1-\beta)\frac{\gamma-1}{2}M_\infty^2}{1+\frac{\gamma-1}{2}M_\infty^2} \quad (18)$$

where β is the aerodynamic recovery factor of the thermocouple base. A baseline value of 0.98 was assumed for β based on the literature. The heat transfer coefficient of the thermocouple may be calculated as:

$$h_c = \frac{k_f Nu}{d_w} \quad (19)$$

where $k_f$ is the thermal conductivity of air and Nu is the Nusselt number, determined by Moffat [21] using a curve-fit for experimental data of flow parallel to the wire:

$$Nu = 0.85 Re^{0.674} \text{ [9]} \quad (20)$$

The Reynolds number can be calculated based on the environmental conditions within the stagnation tube and the thermocouple wire diameter as:

$$Re = \frac{10.08 d_w M_1 P_t}{\mu_e \sqrt{T_0}} \quad (21)$$

The viscosity of air can be calculated from total temperature using the Sutherland formula as:

$$\mu_e = \frac{b T_0^{3/2}}{T_0 + S} \quad (22)$$

where b and S are constants and equal to 1.458e-6 kg/(m∗s∗K$^{1/2}$ ) and 110.6K respectively. This equation can be found in any Boundary Layer textbook.

## 2.2.4 Radiative Error

At low temperatures, such as the room temperature used in this analysis, radiative effects will have very little effect on the overall recovery. However, for rigor and to enable applications at higher temperatures, it is included in the analysis. The radiation

component error can be derived from the Stefan-Boltzmann Law and is presented in Moffat [21] as:

$$T_0 - T_r = 1 - \frac{T_r}{T_0} = \frac{K_R \sigma \varepsilon A_R \left(T_J^4 - T_W^4\right)}{h_c A_c} \tag{23}$$

which can be put in terms of the other temperature ratios:

$$1 - \frac{T_r}{T_0} = \frac{K_R \sigma \varepsilon A_R}{h_c A_c} \left[ \left[ T_0 \left( \frac{T_v}{T_0} - \frac{T_c}{T_0} - 1 \right) \right]^4 - \left[ T_0 \left( \frac{T_w}{T_0} \right) \right]^4 \right] \tag{24}$$

where $K_R$ is the radiation form factor, σ is the Stefan-Boltzmann constant, ε is the emissivity, $A_R$ is the area available for radiative heat transfer, Ac is the area available for convective heat transfer, and:

$$1 - \frac{T_w}{T_0} = \frac{(1-\kappa)\frac{\gamma-1}{2} M^2}{1+\frac{\gamma-1}{2} M^2} \tag{25}$$

where κ is the aerodynamic recovery factor of the stagnation tube. A baseline value of 0.96 was assumed for κ based on the literature. Although this value is given for a tube and not an airfoil, the interior shape where the radiation has the greatest effect has a tube shape.

### 2.2.5 A Note on Recovery Factors

The convective portion of the recovery ratio equations discussed in this chapter is based upon the assumption that the fluid is brought to rest adiabatically to measure the total temperature and thus the total energy. In real flows, a portion of the kinetic energy of the flow is lost during the conversion to thermal energy, which is accounted for in these equations using the aerodynamic recovery factor of the thermocouple, α. The portion of

the flow that is lost is primarily dependent on two factors. The first is the geometry of the section of the sensor that is exposed to the flow. The second is the flow over the sensor; a higher flow velocity results in a greater amount of kinetic energy that must be converted and a greater opportunity for some of that energy to be lost and therefore a lower value for the aerodynamic recovery factor of the thermocouple. The internal flow velocity can be easily calculated from the continuity equation, the area ratio, and the freestream velocity if the assumption is made that the flow is incompressible.

The conductive portion of the recovery ratio equations involves the assumption that the material that forms the shroud of the sensor and connects to the thermocouple does not affect the temperature measured by the thermocouple. In real situations, the temperature of any material in contact with the thermocouple will have an effect. This effect is accounted for by the aerodynamic recovery factor of the thermocouple base, β. The thermocouple base is defined as the point where the thermocouple attaches to the structure of the sensor. The temperature of the surrounding material is influenced by several factors; the most relevant in this situation is the flow over the interior and exterior of the sensor. The other factors, such as ambient temperature, will act to drive the temperature away from the temperature of the flow, but are approximately consistent for all probes. The flow over the interior of the sensor will act to drive the temperature of the sensor material to the same temperature as the thermocouple and is affected by the velocity of the flow. Flow over the exterior of the sensor will act in a similar manner but will not have a significant effect in the short term due to the thickness of material separating the interior flow channel from the exterior surface. A higher flow velocity will generally result in a wall temperature that is closer to that of the flow. A decrease in the difference between the temperatures of the thermocouple and the wall of the flow channel that forms the base of the thermocouple will result in a value closer to unity for the recovery factor of the thermocouple base. It has been noted by Tommasini [31] that the recovery ratio equations are more sensitive to this aerodynamic recovery factor than to the other two.

## *2.3 Higher Order Corrections*

The lower order model is expected to be accurate to within the range of condition limitations, but a higher accuracy model was desired if one could be developed. It was determined that a few minor additions could be made to the model that did not greatly affect computational cost but which improved the fidelity of the model.

### 2.3.1 Aerodynamic Recovery Factors

In the lower order base model, recovery factors were assumed to be constant. In reality the recovery factors are dependent on a number of parameters, most notably yaw, Reynolds number, and Prandtl number [31]. For this analysis, Prandtl number does not vary significantly.

#### *2.3.1.1 Variation in Yaw*

The thermocouple aerodynamic recovery factor, α, has been proven to have negligible variance with Reynolds number in subsonic conditions. [8 & 10] However, it has been shown to have significant variance with yaw. For flow parallel and normal to the axes of the thermocouple, the following values are recommended [21]:

$$parallel: \ \ \alpha = 0.86 \ \pm 0.09$$
$$normal: \ \ \alpha = 0.68 \ \pm 0.07$$

A search of available literature yielded no information on the recovery factor for the angles in between zero and ninety degrees so a simple linear fit was assumed. Very little information is available on the effect of yaw and Reynolds number on the other two recovery factors, though the recovery factor of the thermocouple base, β, is known to vary with both[31]. A fairly simple model was implemented that assumed a linear variation with yaw with the same slope as α and zero degree values equal to the baseline values. This is expressed mathematically as:

$$\alpha(yaw) = \alpha|_{@yaw=0} + slope * yaw \qquad (26)$$

with the slope equal for all three recovery factors. This model is very simplistic and is only valid due to the low order of the analysis. Further analysis beyond the scope of this study would be required to determine a more accurate approach.

#### *2.3.1.2 Variation between sensor designs*

It has often been noted that determination of the recovery factors must be done experimentally for each new design [21, 31]. In the lower order base model the assumption is made that the variations in geometry between the probe designs have no effect on the three aerodynamic recovery factors. While this is a reasonable assumption for a lower order analysis, it is not an accurate reflection of the reality. Differences in the geometry affect the internal flow through the sensor, which can have significant effects on the recovery factors of the thermocouple and thermocouple base as discussed in Section 2.2.5. For instance, an increase in the inlet capture area created by the chamfer will increase the mass flow rate through the sensor which will result in a higher internal flow velocity than an unchamfered sensor. As discussed in Section 2.2.5, a higher internal velocity will result in a lower value for the aerodynamic recovery factor of the thermocouple and a value closer to unity for the aerodynamic recovery factor of the thermocouple base. A decrease in the bleed hole to inlet area ratio will have a similar effect. This supports the argument that the recovery factors must be determined for each individual sensor design.

### 2.3.2 Karman-Tsien Compressibility Correction

The linear vortex panel method assumes ideal flow, which greatly simplifies the analysis and is valid in a variety of real applications. Ideal flows are irrotational and incompressible. While strictly ideal flows are rare in practical situations, the assumptions are valid for certain types of flows or for lower order analysis such as this. Inviscid analyses of a lifting body with a sharp trailing edge produce an infinite number of solutions corresponding to various circulation values. In order to select the proper, unique solution, a particular viscous effect is accounted for using the Kutta Condition,

which is standard in this type of analysis. The Kutta Condition places the rear stagnation point at the trailing edge and accounts for the loss of momentum through friction experienced by viscous flow on the underside of the body which prevents the flow from negotiating the sharp turn at the trailing edge which then causes the flow to separate. Compressibility can also be partially corrected for relatively easily using a correction factor. Several correction factors were developed to adapt low-speed aerodynamic results to high-speed subsonic flight to account for local compressible effects, in the regime of $M_\infty<0.7$. The most well-known compressibility correction factor is the Prandtl-Glauert rule, however better models exist. The Karman-Tsien rule is one such model and is used in this analysis. It uses the freestream Mach number to correct the coefficient of pressure as:

$$C_p = \frac{C_{p_0}}{\sqrt{1-M_\infty^2}+\left[\left(\frac{M_\infty^2}{1+\sqrt{1-M_\infty^2}}\right)\frac{C_{p_0}}{2}\right]} \tag{27}$$

where $C_{p_0}$ is the ideal flow coefficient of pressure. For higher Mach number flows, this correction factor becomes more important in predicting actual flow. More information about compressibility corrections and the Karman-Tsien rule can be found in any number of Aerodynamics textbooks (such as Fundamentals of Aerodynamics and Modern Compressible Flow, both by John D. Anderson).

### 2.3.3 Paneling

A relatively simple method of improving the fidelity of the model would be to change the paneling used in the linear vortex panel method. An increase in the number of panels would increase the resolution of the flow model and increase fidelity; however, it would also increase computational cost. A method that would increase accuracy without increasing computational cost would be to concentrate the paneling at the leading edge, trailing edge, and bleed hole locations as those are the areas of most

interest. Given the difficulty in repaneling the sensor, however, this method was not implemented in this analysis.

## *2.4 Validation of Components of the Model*

Since an extensive search of available literature yielded no data for embedded Shielded sensors to use in validating the model, model validation was done in three distinct parts. First, the recovery correction factor equations were validated using data for traditional Shielded sensors. After the linear vortex panel method was implemented, it underwent validation. Finally, the model was used to design sensors which were tested to fully validate the model. This last stage of validation will be discussed further in Chapter 4.

### 2.4.1 Validation of the Recovery Ratio Equations

As a first step towards model validation, the recovery correction factor equations, which had been algebraically manipulated into a different form than is available in Moffat [21] and are detailed in Chapter 2, were compared to available data. One of the primary data sources used to validate this portion of the model is the experiments performed by Willbanks [34] in the early 1970s. That report contains data for a traditional Shielded probe tested at several pressures and Mach numbers. Only data for three of the pressures was used in the validation as the other two pressures were outside the range of interest in this analysis. While all of the geometric parameters were provided in the report, the recovery factors and the bleed discharge coefficient, which are generally determined experimentally, were not provided and had to be determined. As shown in Figure 2.3, a good fit with the data was achieved using the following parameters: $r_b = 0.86, r_s = 0.88, r_t = 0.85,$ and $C_d = 0.20$, which are in the range of typical values for Shielded probes. [21]

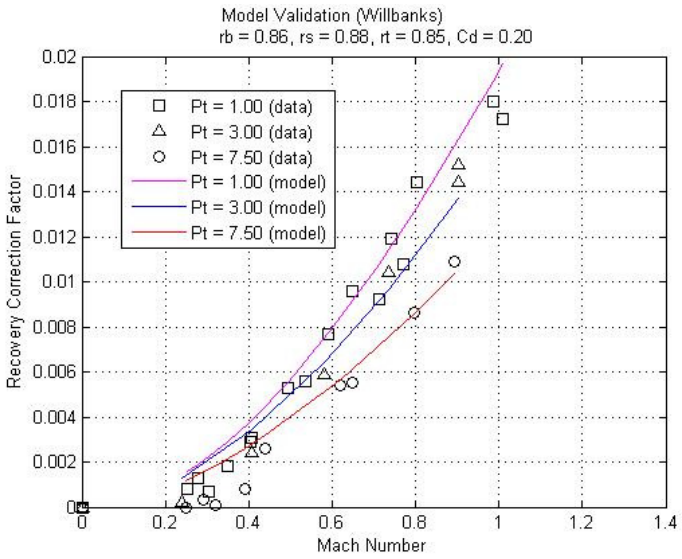


**Figure 2.3. Comparison of the recovery correction factor equations (lines) to the data obtained by Willbanks (points).**

The model achieves an excellent match to the data for Mach numbers above 0.4. While the model is less accurate for Mach numbers between 0.2 and 0.4, the difference is on the order of $10^{-3}$.

## 2.4.2 Validation of Panel Method

At early stages during the creation of the model, results were compared to data available in the literature for traditional shielded probes. Once the aerodynamic effects were added in, such a validation was no longer possible. However, certain pieces of the model could be validated individually. The pressure coefficients, calculated using the linear vortex panel method, were validated using the widely available Xfoil program.

### *2.4.2.1 Xfoil*

Xfoil is a program developed in the 1980s used for the design and analysis of subsonic isolated airfoils. Allowing the calculation of both inviscid and viscous flow, it has a fairly wide range of useful analytical capabilities including forced or free transition, Karman-Tsien compressibility correction, and fixed or varying Reynolds and/or Mach numbers. While the program is a bit clunky to use, it is an excellent mid-range analysis tool. It

utilizes a linear vortex panel method but extends the paneling to the airfoil wake and also includes a source sheet on the airfoil surface and wake [9]. These additions allow for higher accuracy and the inclusion of viscous effects.

#### *2.4.2.2 Comparison*

Since xfoil uses a linear vortex panel method very similar to the one implemented in the model, the results should be nearly identical. Xfoil is used only for validation and is not implemented in the code due to the increased computational cost associated with its use and the inherent difficulties communicating with the rest of the code.

As this portion of the model is focused on the aerodynamics of the sensor, validation is conducted by comparing the aerodynamic quantities produced by each model. These aerodynamic quantities include the coefficient of pressure and the coefficient of lift.

The coefficient of pressure distribution along the airfoil was plotted for each method at several yaw angles and compared. These distributions are shown below for three select angles. Additionally, the coefficient of lift was calculated from the pressure distributions at the several yaw angles and compared between models. This figure is also shown below.

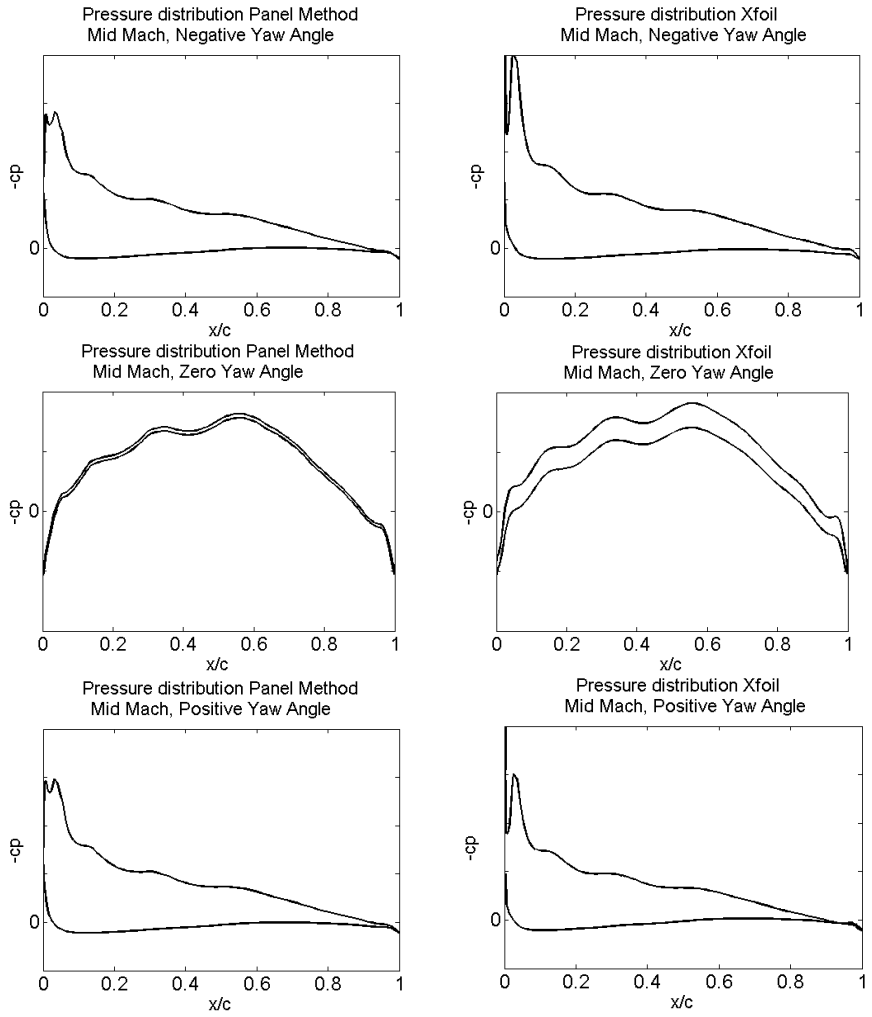


**Figure 2.4 Pressure distribution linear vortex panel method (left) vs xfoil (right) for select parameter set at three yaw angles.**

The comparison between the methods was performed for several sets of desired parameters to confirm validity for all sets. An example is shown below in Figure 2.5. Both methods predict very similar results, although the linear vortex panel method used in this analysis predicts higher lift coefficients than xfoil.

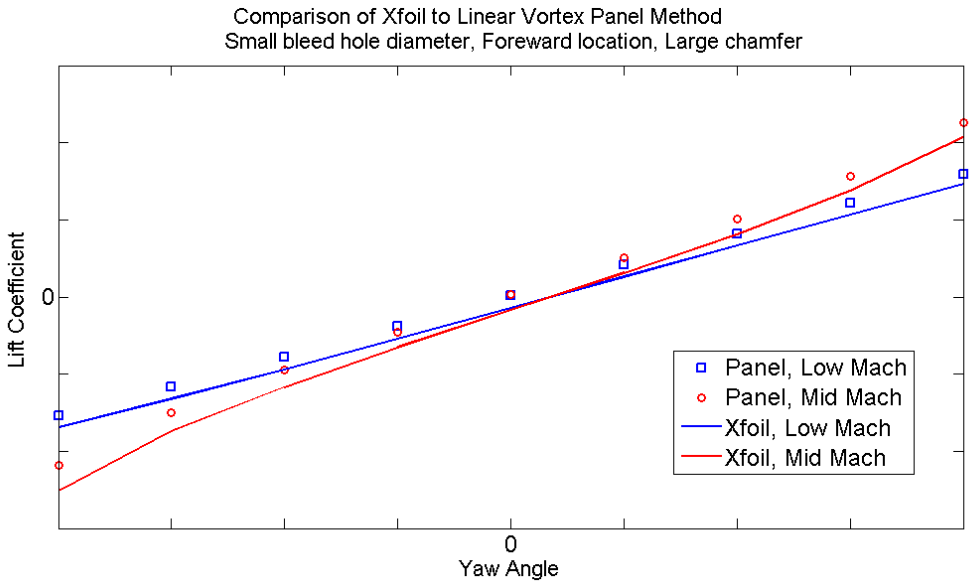


**Figure 2.5 Lift coefficient vs yaw angle for linear vortex panel method and xfoil.**

Both models predict very similar results that allow for the conclusion that the linear vortex panel method is as valid in its calculations for these conditions as xfoil is.

# Chapter 3: Validation Experiment Setup

## 3.1.1 Facility

Full details of the Hot Jet Facility can be found be found in Brooks et al. [Brooks_2014]. Of primary concern to this analysis is the flow that is produced by the facility. The facility, shown in Figure 3.1, is fed by a by an air compressor with a total volume of 23 $m^3$ which allows the facility to be run continuously up to a Mach number of 2.

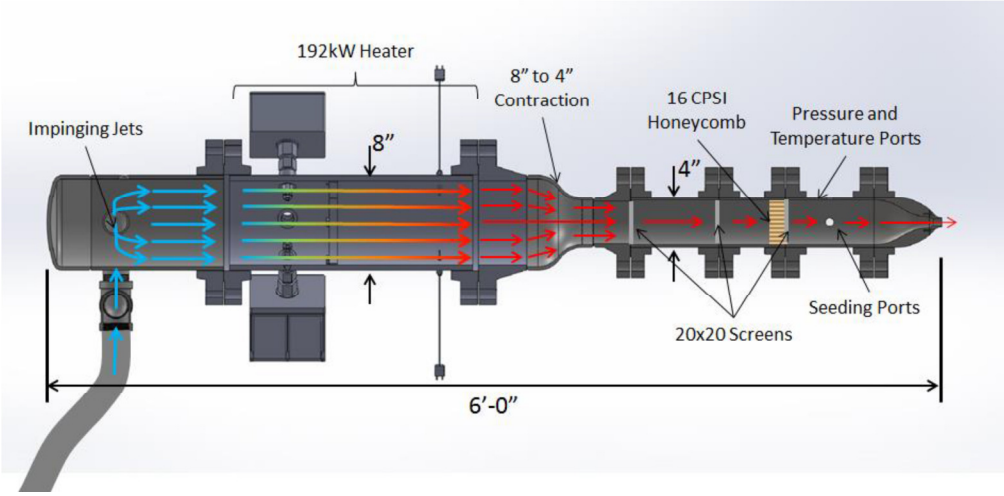


**Figure 3.1 Overview diagram of the supersonic hot jet facility detailing the flow conditioning used**.

The facility was built to allow the air to be heated; although that function was not used in this analysis, it could prove useful in further analysis. The test rig, not shown in this figure, was located 1 inch downstream of the nozzle outlet.

## 3.1.2 Data Collection

Determination of the recovery correction factor requires two key measurements: plenum reference temperature and the temperature measured by the sensor. Since the temperature measured by the sensor is used in the formula for recovery correction factor as part of the difference between the reference temperature and the temperature of the sensor under test, this difference was measured directly rather than each component measured separately. Measurement was performed using an Agilent

34420A nanovoltmeter, due to the small magnitude of the voltages being measured. Figure 3.2 shows the setup used for the measurements. Early testing was performed with a bare wire thermocouple inserted perpendicular to the flow for the plenum temperature measurements. This configuration required the use of a correction factor, detailed in section 3.3.3. This thermocouple was later replaced with a thermocouple in a Kiel type configuration, which eliminated the need for that correction factor.

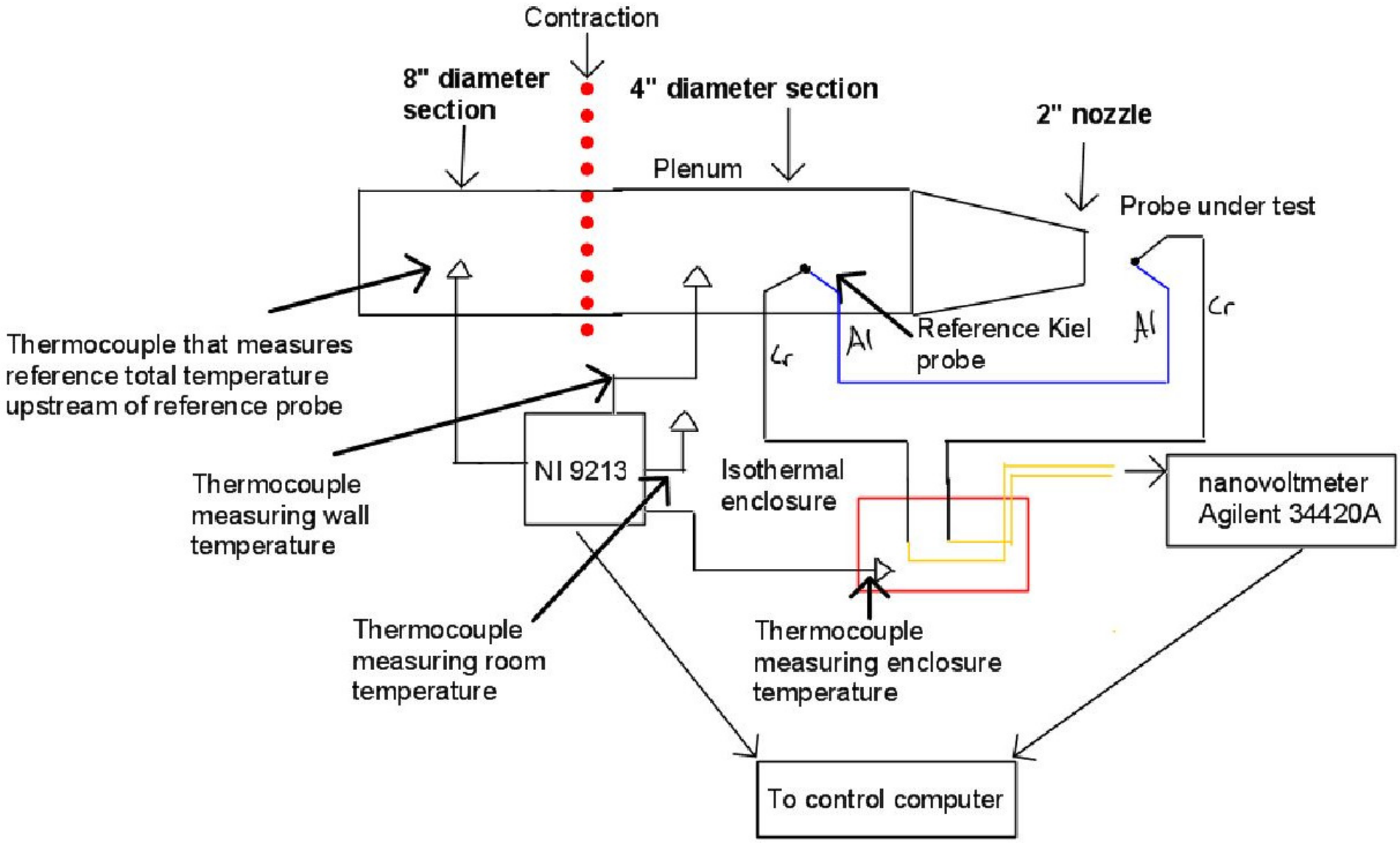


**Figure 3.2. Overview of the experimental setup depicting the type and approximate location of all sensors used**

In addition to the two required measurements, several other measurements were obtained as part of a test for correlation to ambient conditions. These additional measurements, also depicted in Figure 3.2, are the ambient room temperature, the wall temperature of the plenum section of the jet, and the temperature inside the insulated enclosure containing the thermocouple-voltmeter junctions. These measurements were collected using an NI 9213 16 channel module with built in CJC. Conversion of the measured voltages to temperatures was performed automatically in the LabVIEW code used for data collection.

### 3.1.3 Data Processing

Once the raw data is gathered, it must be processed to the point where it can be compared to the analytical model. While quite a lot of data is gathered regarding the quality of the flow, the primary measurements relevant to this analysis are the temperature of the plenum, well upstream of the sensor, and the difference in temperature between the plenum temperature and the sensor under test. Both are measured as voltages and converted to temperatures using the following two equations:

$$T_{measured}(K) = \left[mean\left(T_{measured}(F)\right) - 32\right] \times \frac{5}{9} + 273.15$$

$$\Delta T(K) = T_{sensor} - T_{measured} = \frac{mean(\Delta V(V))}{22.611e-6} \times \frac{5}{9} \quad (28)$$

where $T_{measured}$(K) is the plenum temperature in Kelvin, $T_{measured}$(F) is the plenum temperature in Fahrenheit, ΔV(V) is the voltage that measure the temperature difference, and the constants are the ones necessary to make the conversion.
From these parameters the recovery ratio can be calculated as:

$$R = \frac{T_{sensor}}{T_{measured}} = \frac{T_{sensor} - T_{measured} + T_{measured}}{T_{measured}} = \frac{\Delta T(K)}{T_{measured}(K)} + 1 \quad (29)$$

Early measurements were taken with the plenum thermocouple perpendicular to the flow due to facility constraints, so a correction factor was introduced to account for it. This correction is dependent on the Mach number and is based on the aerodynamic recovery equation:

$$T_{measured} = T_t \left[ 1 - \frac{(1-\alpha)\left[\frac{\gamma-1}{2}\right] M_{plenum}^2}{1+\left[\frac{\gamma-1}{2}\right] M_{plenum}^2} \right] \tag{30}$$

where $\alpha$ is set at 0.68, the value suggested by Moffat and others for wires normal to the flow, and $M_{plenum}$ is the Mach number computed from area ratios of the flow within the plenum:

$$\frac{A_{jet}}{A_{plenum}} = \frac{1}{4} = \frac{M_{plenum}}{M_{jet}} \left( \frac{\left[1-\frac{\gamma-1}{2} M_{jet}^2\right]}{\left[1-\frac{\gamma-1}{2} M_{plenum}^2\right]} \right)^{\frac{\gamma+1}{2(\gamma-1)}} \tag{31}$$

Since a solution to $M_{plenum}$ as a function of $M_{jet}$ is not readily obtainable, a curve fit is used to calculate $R_{plenum}$. From this value for $R_{plenum}$, the corrected recovery ratio can be calculated as:

$$R_{corrected} = \frac{T_{sensor}}{T_t} = \frac{T_{sensor}}{T_{measured}} \frac{T_{measured}}{T_t} = R_{plenum} \left( \frac{\Delta T}{T_{measured}} + 1 \right) \tag{32}$$

Later testing was performed using a thermocouple in a Kiel type configuration, which eliminated the need for this correction factor.

# Chapter 4: Experimental Validation Results

## *4.1 Validation of Model*

A low order model consisting of a panel method probe aerodynamics model that feeds into a zero-order thermodynamics model was developed to aid in the design of embedded Shielded sensors. This model required validation through physical testing using sensors which were created to test the effects of three geometric parameters on the performance of the sensors. Validation of the model was performed by comparing the experimental data obtained to the model predictions for the geometric parameters. A good match between the experimental data and the model validates the model for the conditions tested. If an offset is present, it may indicate the existence of physical phenomena not well represented in the model. Yaw and Mach calibrations were performed for all of the sensors to determine their performance. Pitch calibrations were also performed for select probes to analyze the effect of pitch to assist in the effort to expand the model to include pitch.

For the purposes of comparison, probe and sensor conditions are changed with respect to Mach number (and by virtue of the free jet, Reynolds number), yaw angle and pitch angle. Unless otherwise specified, only one of these parameters is varied from the default at a time, to more accurately determine the effect of each. The effect of coupled parameters is not within the scope of this study. The default parameters are: middle or mid Mach number, 0 degree pitch, 0 degree yaw.

Select higher order corrections, discussed in Chapters 2 & 3, are included in the analysis, namely the Karmen-Tsien compressibility correction and the linearly varying recovery factors. Although the Karmen-Tsien compressibility correction has greatest effect at the high Mach number, there is still some effect on the middle Mach number that is worth consideration. The slope of the linearly varying recovery factors was chosen based on Moffat's analysis [21], detailed in Section 2.3.1. According to Moffat and other sources,

the baseline values for the individual recovery factors cannot be calculated analytically and must be determined experimentally or computed with high fidelity methods such as CFD, representing one of the major uncertainties of the current model. These factors were varied in the model between the limits available in literature [21] in order to achieve a good match to the experimental data. Further refinements of these recovery factors, such as by using future-available CFD results, may achieve a more satisfactory match to the data.

### 4.1.1 Effect of Bleed Hole Diameter

The low order analysis used in the model predicts that the effect of bleed hole is most dramatic for the largest diameter bleed hole. As is evident in Figure 4.1, this is indeed the case. There is a significant gap between the zero degree offset of the recovery of the large bleed hole compared to the other two, as is predicted by the model. Also as predicted by the model, the smallest diameter bleed hole has the most favorable 0 degree yaw recovery, and a steeper slope than the medium bleed hole. In terms of the trends predicted, the model is accurate.

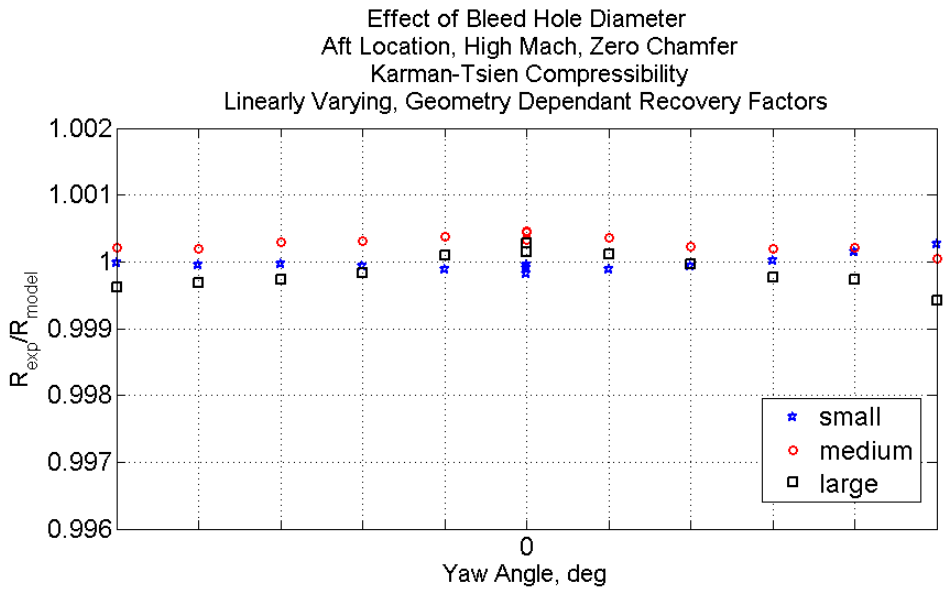


**Figure 4.1. Comparison between model prediction and experimental data vs yaw angle for bleed hole diameter. Data is presented as the ratio of the experimental data to the model prediction. The model prediction includes the Karmen-Tsien compressibility correction and the linearly varying, geometry dependent recovery factors discussed in Chapter 2.**

Similar to the results for yaw angle, the results for Mach number show a good match to the trends predicted by the model, shown in Figure 4.2. Comparison between model prediction and experimental data versus Mach number for bleed hole diameter. As with the results for yaw angle, however, there is still a significant offset for recovery of the large bleed hole diameter sensors. This offset increases with increasing Mach number, rendering the model more accurate at low Mach numbers than at higher Mach numbers.

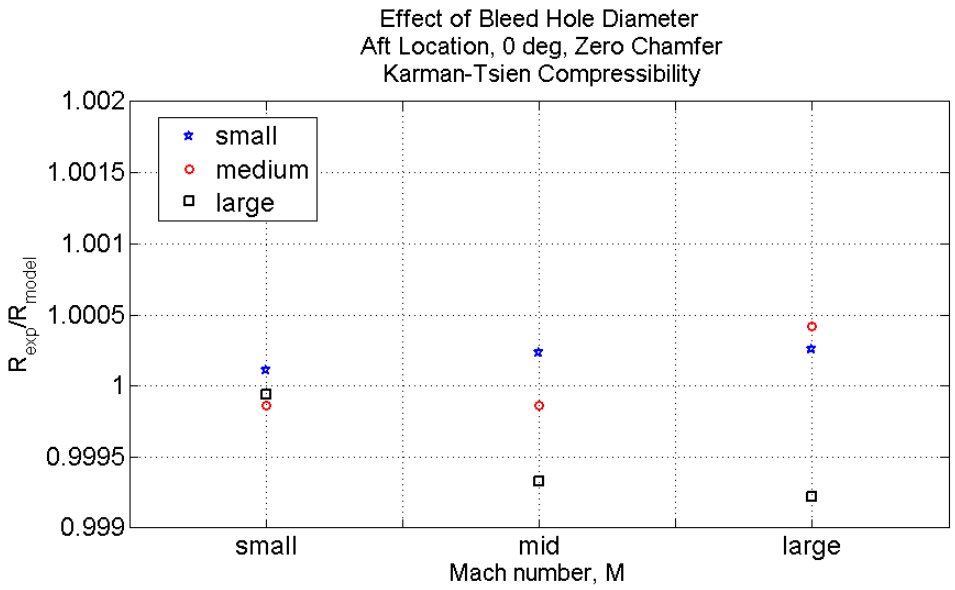


**Figure 4.2. Comparison between model prediction and experimental data versus Mach number for bleed hole diameter. Data is presented as the ratio of the experimental data to the model prediction. The model prediction includes the Karmen-Tsien compressibility correction and the linearly varying recovery factors discussed in Chapter 2.**

The model, however, also predicts a tighter spread for the data than is present in the experimental setup, likely caused by a greater influence of conduction in the model than is present in the actual sensors. Radiation has little effect on the recovery at the temperature of current interest. This is likely due to the model being designed for metal sensors and the experiment using 3D printed plastic sensors due to cost. Either way, the trends match fairly well between the data and the model, so the model may still be used as a comparative predictor for the effects of bleed hole diameter. The model may be considered valid with the caveat that it is highly advised to perform physical testing to ensure accuracy of results, particularly for sensors with bleed hole diameter near the upper or lower limits.

### 4.1.2 Effect of Bleed Hole Location

The predictions made by the low-order model for the effect of bleed hole location is that the forward bleed hole would be more sensitive to yaw and therefore have a smaller useable range. As shown in Figure 4.3, this trend is also seen in the data, though

not as dramatically. While the recovery for the aft location remains fairly constant across this yaw range, the recovery of the forward location remains constant over a smaller range centered around 0 degrees.

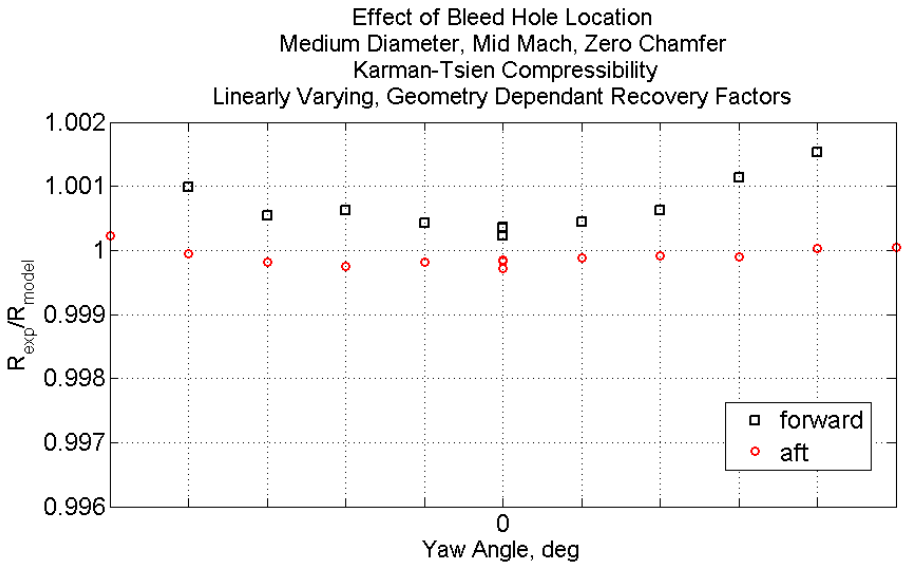


**Figure 4.3. Comparison of model prediction to experimental data versus yaw angle for bleed hole location. Data is presented as the ratio of the experimental data to the model prediction. The model prediction includes the Karmen-Tsien compressibility correction and the linearly varying, geometry dependent recovery factors discussed in Chapter 2. Further refinement individual recovery factors for the forward bleed hole geometry will improve the match to the results.**

As is also evident, there is a much closer match between the model and the experimental data, although the model again predicts a tighter spread. It is apparent that whatever element of the aerodynamics or test setup affecting the bleed hole diameter comparison has little effect on the bleed hole location with respect to yaw. The differences between the model and the experimental data are more pronounced in recovery that varies with Mach number rather than yaw angle, as seen in Figure 4.4. The forward location shows good match between the model and the data for all three Mach numbers of interest. The aft bleed hole, does not behave as predicted by the model, increasing more significantly with Mach number than is predicted. This behavior may be

the result of the very-low-order treatment of the inlet chamfer, which would have greater effect at higher Mach number and higher yaw angles. The effect of the chamfer would be to lessen the variation of recovery with yaw and Mach, as is clearly seen in both figures.

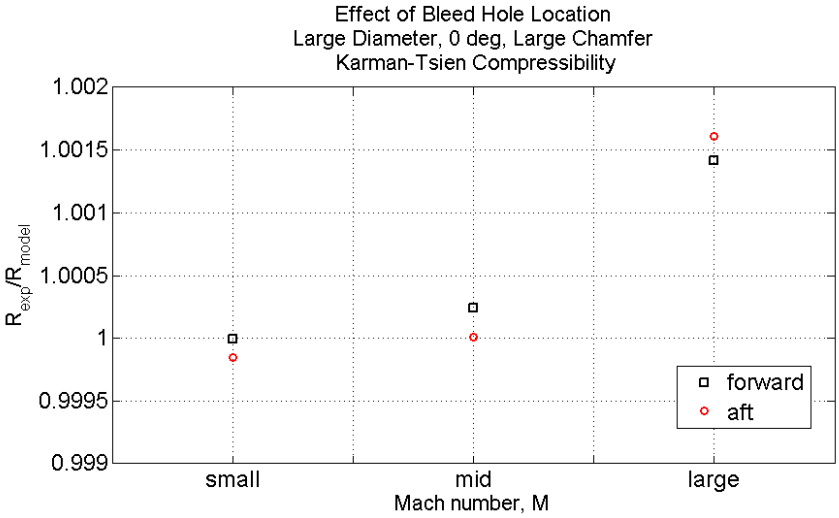


**Figure 4.4. Comparison of model prediction to experimental data versus Mach number for bleed hole location. Data is presented as the ratio of the experimental data to the model prediction. The model prediction includes the Karmen-Tsien compressibility correction and the linearly varying recovery factors discussed in Chapter 2.**

It is evident, however, that the model does not account for the separation effects which greatly influence the aerodynamics and thus the recovery. The separation effects are most noticeable when comparing the recovery for different bleed hole locations because the effect changes along the airfoil in the streamwise direction. From this the conclusion can be drawn that this element of the aerodynamics not well accounted for in the model is the cause of the discrepancies between the model and the data seen in Section 4.1.1. The model is fairly accurate for the bleed hole location and may be considered valid for the between the limits of the two locations.

### 4.1.3 Effect of Inlet Chamfer

The effect of inlet chamfer predicted by the model was to increase the yaw range by reducing the sensitivity to changes in angle at higher yaw angles. It is predicted that the chamfer will have no effect on the recovery at yaw angles closer to zero degrees. The experimental data bears out this prediction fairly well for the medium and large chamfers, as shown in Figure 4.5. The large offset visible in the small chamfer is likely due to separation at the inlet due to the sharpness of the inlet edge which is not accounted for in the model.

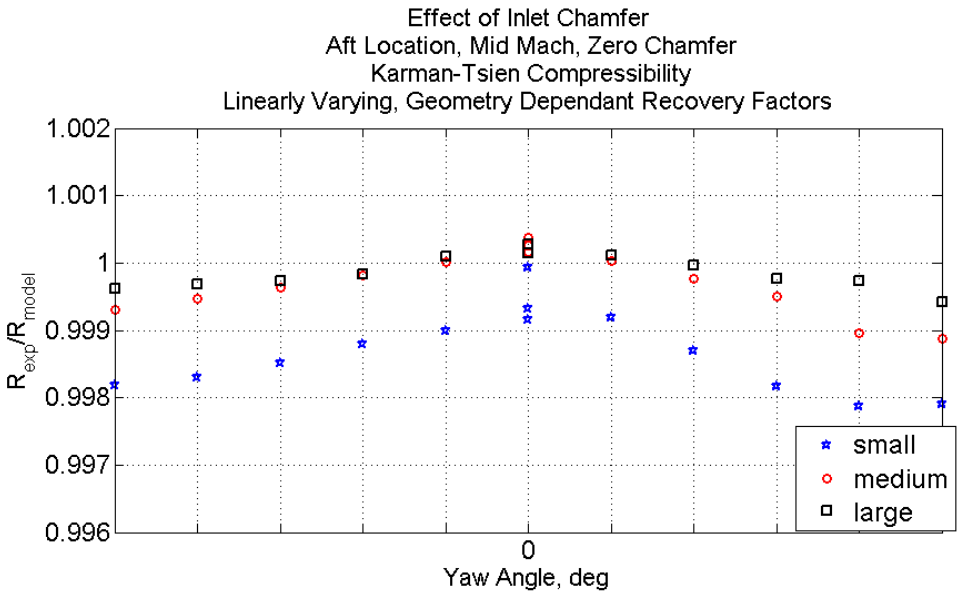


**Figure 4.5. Comparison of model predictions to experimental data versus yaw angle for inlet chamfer. Data is presented as the ratio of the experimental data to the model prediction. The model prediction includes the Karmen-Tsien compressibility correction and the linearly varying, geometry dependent recovery factors discussed in Chapter 2.**

The variation of recovery with Mach number is not shown as model fidelity is insufficient to capture any chamfer effects at zero degrees yaw. It has been suggested that the lack of chamfer represented by the small chamfer could result in multiple modes of separation on the inlet. This could be responsible for the offset and the asymmetry of the recovery compared to the model, but would require further analysis

beyond the scope of this study. Overall, the data matches the model reasonably well, so the model may be considered valid for chamfer predictions between the limits of the medium and large chamfers.

## *4.2 Pitch angle results*

In addition to validating the model, the data presented above supports the hypothesis that aerodynamic effects dominate the recovery. Further evidence of the effect of the aerodynamics of the sensor on the recovery may be observed in the pitch angle recovery. Included in this analysis to help incorporate the effects of pitch in the model, the results of recovery variation with pitch angle also support the hypothesis that aerodynamic effects dominate the recovery. If the hypothesis is correct, it is expected that recovery will initially increase due to decreased mass flow rate at the sensor inlet and then decrease sharply once the pitch angle is too steep to allow sufficient mass flow through the inlet. It is also expected that sensors with a large inlet chamfer will decrease sharply at a larger angle of pitch due to the chamfer diverting air into the inlet. For this study, the analysis of pitch was performed using the angle at which the recovery drops below 0.1% of its maximum value as the key performance parameter. This angle is indicative of the angle at which there is insufficient mass flow through the inlet to maintain steady convective heat transfer. At this point, aerodynamic effects no longer dominate the recovery and the recovery drops significantly. The results for selected sensors are provided in Table 4.1.

**Table 4.1. Pitch angle recovery results compared to geometric parameters.**

| Bleed Hole Diameter | Bleed Hole Location | Inlet Chamfer | Angle of 0.1% recovery |
|---|---|---|---|
| Medium | Forward | Large | Medium |
| Large | Aft | Medium | Low |
| Large | Forward | Large | High |
| Large | Aft | Large | High |

From these results it is clear that the aerodynamics of the sensor have a significant influence on the recovery. Geometric parameters which result in a high mass flow rate have the most favorable pitch angle recovery. Large diameter bleed holes and a large inlet chamfer are the major contributors to a high mass flow rate. Although a high mass flow rate tends to increase the recovery correction factor and therefore decrease recovery in respect to both Mach number and yaw angle, it improves the pitch angle characteristics of the sensors. A trade-off must therefore be made if a greater pitch range is desired.

## *4.3 Corrections*

Several corrections have been suggested to improve the accuracy of the data. Many of these corrections are designed to account for the variable ambient conditions present during tests and between tests of different probes. While such effects are minute and generally are not determined to be worthy of consideration, the precision required for this study is much higher than general studies. For that reason, it is possible that the generally insignificant variations in ambient conditions can have a significant impact on the data and should be accounted for. Since there is difficulty in determining which factors have the greatest influence on the data and should be corrected for, correlation studies were performed on several key factors. Humidity was considered as a possible key factor as it could result in a small EMF around the bead of the thermocouple wire. Since the sensors were made from 3D printed plastic, they could not be grounded as metal sensors are. Outside ambient temperature and pressure were also considered, since the air used in the testing is drawn from outside and those conditions can easily vary significantly over the course of a day. The ambient temperature and pressure inside was also considered, although the inside conditions are partially climate controlled and vary significantly less. The most promising factor considered is the difference between the plenum temperature, which is directly affected by the outside temperature, and the

temperature of the thermocouple junction, which is primarily affected by the inside temperature. It was theorized that this temperature difference might be creating a temperature gradient along the length of the thermocouple wire, resulting in slight artificial variations in the data. As described in Section 3.3.2, additional thermocouples were added to the test setup in order to determine possible correlations. Humidity and pressure were not easily measured; therefore any possible correlation with those factors will require additional analysis beyond the scope of this study.

## *4.4 A note on experimental repeatability*

A significant factor in determining the accuracy of the experimental data, and therefore the accuracy of the model, is the repeatability. If the data is not repeatable, then two possibilities exist. Either there is some error in the experimental setup or there is some condition which changes rapidly between tests. For this study, repeatability is defined in terms of the range of the data collected for multiple tests of the same probe. The range is defined simply as:

$$range = \frac{\max - min}{2} \tag{33}$$

and is calculated at each yaw angle and Mach number used in this study. It is expected that changing ambient conditions, discussed in Section 4.2, will have a small impact on the repeatability of each sensor, and should be approximately the same for all sensors. Figure 4.6 shows the repeatability for the Mach number tests for select sensors. This figure highlights a very noticeable trend that the geometric parameters have a significant impact on the repeatability.

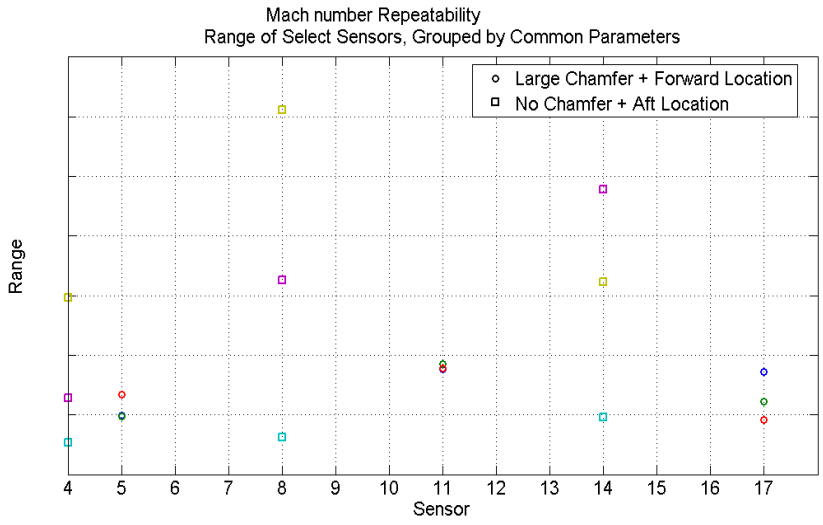


**Figure 4.6. Repeatability of select sensors for Mach number tests. A clear correlation exists between certain geometric parameters and the repeatability.**

It is clear from the data that the inlet chamfer and bleed hole location have a significant impact of the repeatability of the sensors, though it is also appears that there is some effect due to coupling of these parameters. Sensors that have a small or medium chamfer and the bleed holes at the aft location tend to have poor repeatability while sensors that have a large chamfer and a forward bleed hole location have more favorable repeatability. Sensors that have either small/medium inlet chamfer or aft bleed hole location also tend to have poor repeatability, so the coupling effect could be the result of an additive effect of the repeatability.

In an effort to better understand the correlation between repeatability and the geometric parameters, oil flow visualization was performed on several of the sensors. Observations of the oil flow suggested the possibility of multiple steady modes, primarily at the inlet, which would produce significantly different aerodynamics based on minute differences in the flow from the jet. Each mode would result in different recovery characteristics, producing the poor repeatability. Further study would be required to fully understand this phenomenon and incorporate it into the model. In

addition, further investigation beyond the scope of this study would be required to identify and fully understand the effects of geometric parameters on the repeatability.

# Chapter 5: Model Predictions

Once the model had been initially validated, it could be used as a predictive tool for the final stage of validation. The predictions were primarily focused on the effects of the three parameters of interest.

## 5.1.1 Effect of Bleed Hole Diameter

For this low order analysis, the effect of bleed hole is fairly dramatic even though the largest difference is on the order of 10e-4. As shown in Figure 5.1, for the two smaller bleed hole diameters, the primary difference is in the shape of the yaw variance. There is also a noticeable difference in the zero degree yaw value.

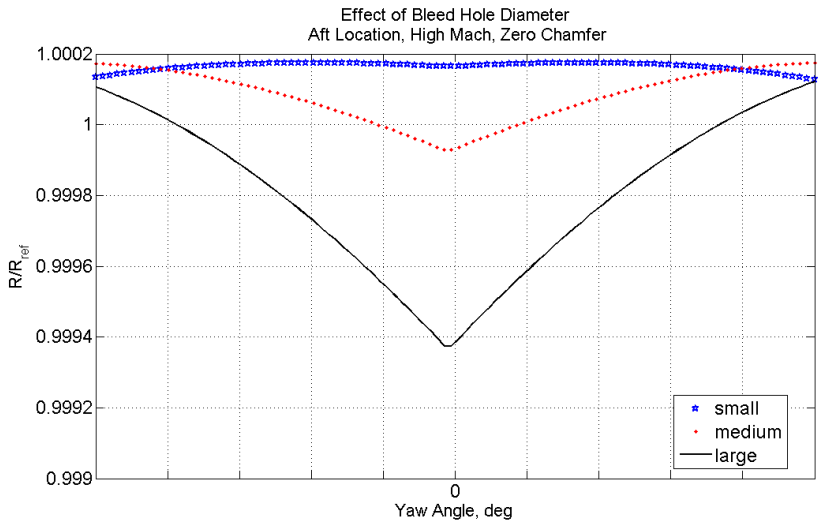


**Figure 5.1. The effect of bleed hole diameter on the yaw angle recovery ratio, as predicted by the model.**

For the large bleed hole, however, there is a very significant difference in both the yaw variance and the zero degree yaw value. Also noteworthy is that the recovery of the large bleed hole is not symmetric around zero degrees yaw. The recovery ratio for the largest bleed hole is symmetric around approximately negative one degree yaw.

The effect of bleed hole diameter on the Mach number characteristics of the recovery are similarly most dramatic for the largest diameter, as shown in Figure 5.2. It is expected that the recovery ratio will decrease with increasing Mach number, due to the increased Mach number at the inlet. As detailed earlier in this report, an increase in the inlet Mach number will result in a decrease in the convective term of the recovery ratio equation.

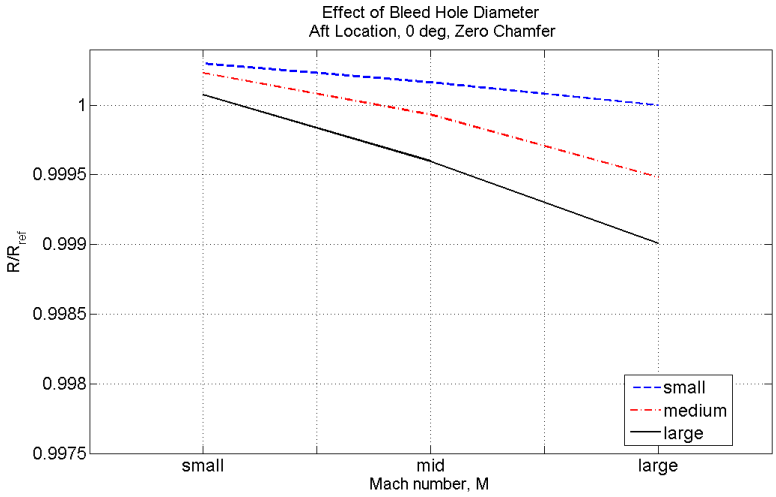


**Figure 5.2. The effect of bleed hole diameter on the Mach number recovery ratio, as predicted by the model.**

This effect is less pronounced for the small and medium bleed hole diameters, resulting in a more favorable Mach number characteristic.

Aerodynamically, these results are due to inlet Mach number. Assuming a constant mass flow rate and density through the sensor, the Mach number of the inlet is directly governed by the area ratio of the inlet to the bleed holes, and therefore, the diameter of the bleed hole. The smaller bleed hole diameter decreases the inlet Mach number, which increases recovery ratio, exactly as shown in the figures above.

### 5.1.2 Effect of Bleed Hole Location

As shown in Figure 5.3 the location of the bleed hole primarily affects the yaw variance and has little effect on the zero degree yaw value. The model predicts that the forward bleed hole results in a higher sensitivity to yaw and a smaller useable yaw range.

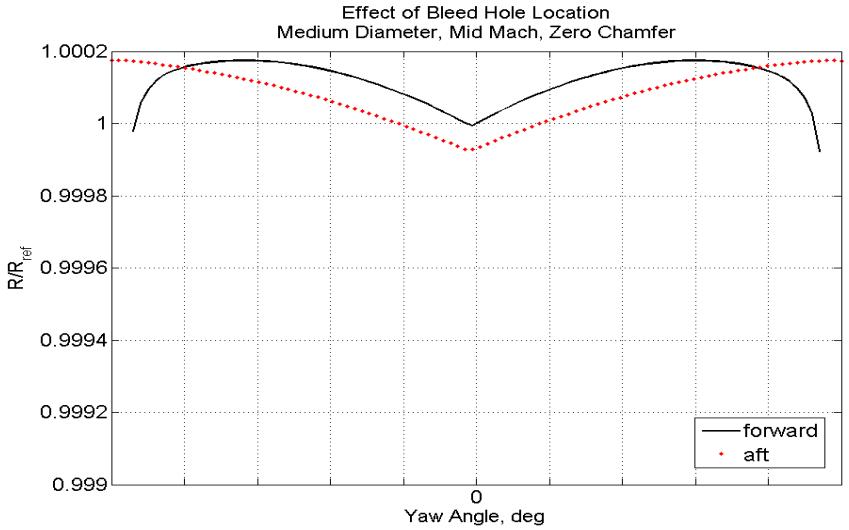


**Figure 5.3. The effect of bleed hole location on the yaw angle recovery ratio, as predicted by the model.**

In contrast to the yaw angle characteristic of the recovery ratio, the Mach number characteristics, shown in Figure 5.4, are not significantly affected by the location of the bleed hole except at Mach = 0.7.

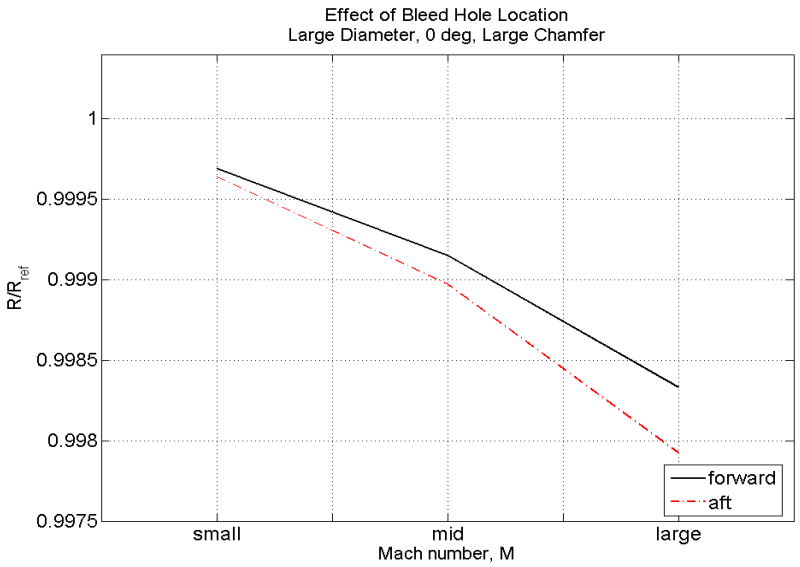


**Figure 5.4. The effect of bleed hole location on the Mach number recovery ratio, as predicted by the model.**

In terms of the aerodynamics, the location of the bleed hole does not have as significant an impact on the inlet Mach number as the diameter of the bleed hole. The location of the bleed hole determines the Mach number at the bleed hole, which is used along with the area ratio to calculate the Mach number at the inlet. The exit Mach number is lower for the forward location which lowers the inlet Mach number as well. As mentioned above, the lower inlet Mach number improves recovery so the forward bleed hole has a higher recovery ratio, at least until the point where the mass flow through the sensor drops too low and aerodynamic effects no longer dominate the recovery, which is noticeable towards extremes of yaw angle.

### 5.1.3 Effect of Inlet Chamfer

The effect of inlet chamfer is not as dramatic as the effects of bleed hole location. The increased chamfer serves primarily to reduce the sensitivity at higher yaw angles. As shown in Figure 5.5, the difference between the chamfer treatments predicted by the model is very minimal and is barely noticeable even at very high yaw angles. This is due to the very low order treatment of the inlet chamfer. The model is insufficient to capture any changes in recovery due to the inlet chamfer at zero degrees yaw, making a comparison to the Mach number calibration useless.

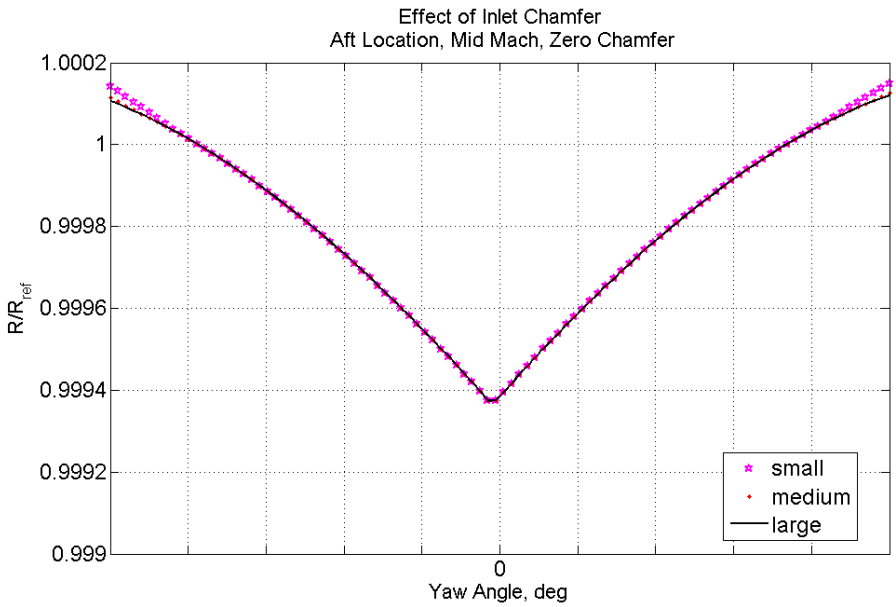


**Figure 5.5. The effect of inlet chamfer on the yaw angle recovery ratio, as predicted by the model.**

Aerodynamically, the effect of the inlet chamfer is to extend the useable yaw range of shielded sensors significantly, as discussed in Gracey [11]. Due to the low order of the analysis, this trend is not well represented.

The effect of inlet chamfer on the aerodynamics is most noticeable at the extremes of yaw angle, where it serves to extend the range of useable yaw angles. An increase in chamfer prevents the mass flow rate from dropping below the threshold for aerodynamic domination of the recovery at quite as low of a yaw angle.

### 5.1.4 Effects of Higher Order Corrections

This analysis relies on a fairly low order model that can be implemented very quickly. Corrections were suggested which would increase the fidelity of the model without greatly increasing computational time or difficulty. These corrections are discussed at length in Chapter 2; however, their effects on the results of the model will be analyzed here.

### *5.1.4.1 Recovery Factors*

Based on the literature, it was suggested that varying the recovery factors with yaw angle would be an appropriate higher order correction. The effect this correction had on the previous results is shown in the subsections below.

#### 5.1.4.1.1 Bleed Hole Diameter

Incorporating the yaw dependency of the recovery factors led to the different bleed hole sizes having significantly more different yaw variance. The effect of bleed hole diameter on the zero degrees yaw value, however, was not affected.

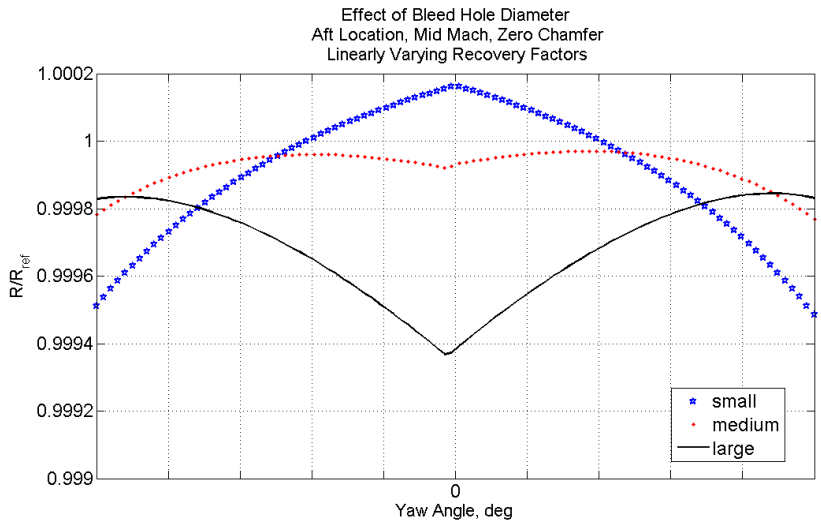


**Figure 5.6. Effect of linearly varying recovery factors correction on the yaw characteristics for bleed hole diameter.**

Allowing a variation of recovery factors based on sensor geometry provides a significantly improved match to the data. Further refinement would allow further improvement, particularly at 0 degrees yaw.

#### 5.1.4.1.2 Bleed Hole Location

Similar to the bleed hole diameter, the incorporation of the yaw dependence of the recovery factors increased the difference in yaw variation between the two bleed hole

locations. However, the trend initially noticed as to which location had greater yaw variance remains unchanged.

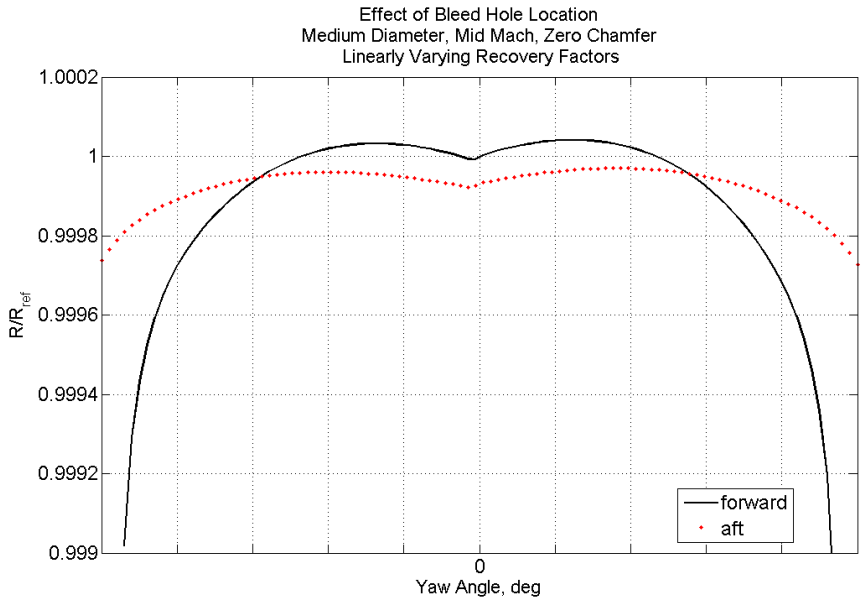


**Figure 5.7. Effect of linearly varying recovery factors correction on the yaw characteristics for bleed hole location.**

#### 5.1.4.1.3 Inlet Chamfer

Incorporating the yaw dependence of the recovery factors into the model had a little effect on the yaw variation of the sensors, as shown in Figure 5.8. Not surprisingly, it did not affect the trend previously noticed about the effect of chamfer on the recovery ratio of the sensor.

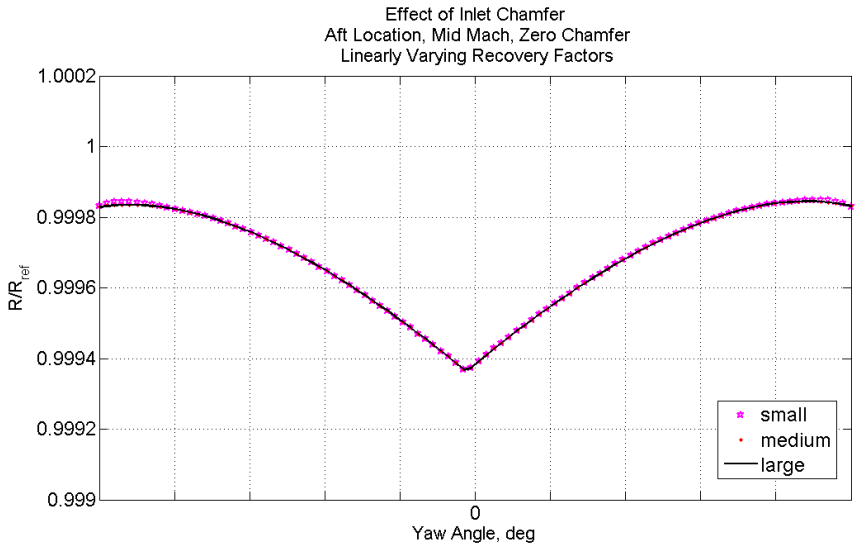


**Figure 5.8. Effect of linearly varying recovery factors correction on the yaw characteristics for inlet chamfer.**

### *5.1.4.2 Karman-Tsien Compressibility Correction*

Since the Karman-Tsien compressibility correction is a function of Mach number, it does not have great effect at the lower Mach numbers. At the high Mach number, the primary effect is to drastically reduce the recovery, as shown in Figure 5.9.

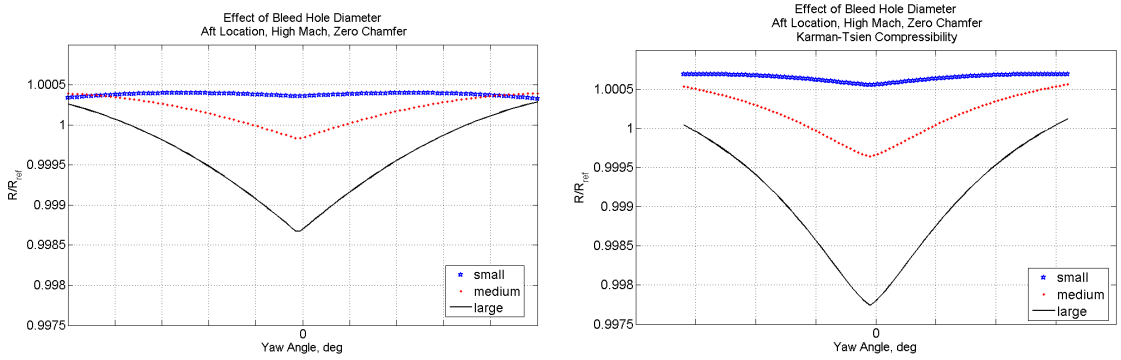


**Figure 5.9. Effect of Karmen-Tsien compressibility correction at high Mach number.**

The inclusion of the Karman-Tsien compressibility correction also alters the shape of the recovery ratio. Accounting for the effects of compressibility, which are very pronounced, must be considered carefully.

## *5.2 Optimal Design*

In order to determine the optimal design, a determination must be made as to what parameters are most highly desired. Given that it is desired to have only one design for a wide range of flow conditions, the ideal sensor would have low variation in recovery ratio over a large range of flow conditions. Experimental data indicates that there are two designs that are optimal based on these criteria. These probes have large inlet chamfer and forward bleed hole location, as well as either small or medium bleed hole diameters. The model predictions identified a third probe as having excellent performance in both pitch and Mach although it performed only slightly above average in the experimental testing. The discrepancy is likely due to the material of the probes. The model was designed based on the end goal of metal sensors while validation and initial testing were performed using less expensive 3D printed plastic probes. This third design has a large inlet chamfer and small bleed hole diameter but has an aft bleed hole location instead of the forward bleed hole location common to the other two designs. At this stage, any of these three designs may be considered ‘optimal’.

Analysis of pitch reveals that probes with excellent pitch and Mach characteristics do not always have the best pitch characteristics, and vice-versa. This suggests that there may not be a design that has excellent characteristics in all three types of flow conditions, requiring trade-off based on desired use, and rendering the title of ‘optimal design’ somewhat meaningless in this context. Further testing and CFD analysis may be able to identify a parameter set that best balances this inherent trade-off.

# Chapter 6: Conclusions

A detailed study has been conducted to create and validate a low-order aerodynamic model for embedded shielded total condition sensors using the Virginia Tech Aerospace and Ocean Engineering Department Hot Jet Facility. While the creation and validation of the model is the primary focus of this thesis, analysis of the aerodynamic characteristics of the embedded sensors is also included. Although Shielded probes are often used in aeroengine testing, no known previous study has been performed involving the novel approach of embedding the Shielded probe directly into the leading edge of a fan blade. This approach is intended to improve the quality of aeroengine testing by reducing the negative effects of the traditional mounting method for shielded probes highlighted in Xiang et al. [37]

The model, which uses an algebraically-manipulated form of the recovery equations presented in Moffat, uses a linear vortex panel method to calculate the aerodynamics of the sensor. Higher order corrections were also suggested to improve the accuracy of the model. Several of these corrections, which take into account compressibility and variance of individual recovery factors, were included in the final model. Other corrections, such as improved paneling for the panel method and the inclusion of pitch angle have not been incorporated at this time but are part of an ongoing effort to improve and expand the capabilities of the model.

The model was validated in three steps, the most important of which was experimental testing of several 3D printed plastic sensors. Quantification of the validity of the developed model was performed primarily by studying the effects of three key geometric parameters on the recovery. These three geometric parameters were determined to have the greatest impact on the aerodynamics and recovery of the embedded Shielded probe. Each parameter had 2-3 selected values encompassing the range of desirable values and sensors were created for every possible combination of these values for use in model validation and to experimentally determine the optimum

combination for low variance recovery. Since fan blades are subjected to a wide range of Mach numbers, yaw angles, and pitch angles, it was desired to determine the design with the lowest variance in recovery across all ranges.

The model was determined to be valid for the range of parameters tested, although with the caveat that not all aerodynamic effects are fully accounted for and physical testing or CFD analysis is advised to verify results once design parameters have been narrowed down sufficiently. These aerodynamic effects and their inclusion in the model are expected to be the topic of further study. In addition, further refinement of the individual recovery factors and investigation into correlation with ambient conditions may increase the accuracy of the model.

Through the course of the experimental validation, a secondary hypothesis was tested that the aerodynamics dominated the recovery. The hypothesis was proved to be correct since the trends in the recovery matched the trends expected based on the aerodynamics of the geometric parameters. A sensor with good aerodynamics will have a favorable recovery. Since this is the case, the profile of the fan blade must be designed carefully to take full advantage of this.

Overall, a model has been created and validated, the aerodynamics of embedded Shielded sensors are better understood, and two optimal designs have been identified for use in aeroengine testing. More study is needed before the embedded sensors can be used to replace traditional total temperature instruments in aeroengine research, but significant strides were made in understanding the behavior of these novel embedded sensors.

# References


1. Annear, J.D., White, H., Holt, S., Power Jets Limited, London, England, U.S. Patent Application for a "Stator Blade Mounting of Condition Sensing Elements in Fluid Flow Machines," no. 295021, filed 9 July 1954.
2. Ashby, D.L., Dudley, M., Iguchi, S.K., "Development and Validation of an Advanced Low-Order Panel Method," NASA TM 101024, Oct. 1988.
3. Bontrager, P.J., "Development of Thermocouple-Type Total Temperature Probes in the Hypersonic Flow Regime," AEDC-TR-69-25, Jan. 1969.
4. Brooks, D.R., Ecker, T., Lowe, K.T., Ng, W., "Experimental Reynolds Stress Spectra in Hot Supersonic Round Jets," AIAA 2014-1227, Jan. 2014.
5. Brouckaert, J.F., "Fast Response Aerodynamic Probes for Measurements in Turbomachines," *Proceedings of the Institution of Mechanical Engineers, Part A: Journal of Power and Energy*, Vol. 221, 2007, pp. 803-813.
6. Buttsworth, D.R., Jones, T.V., Chana, K.S., "Unsteady Total Temperature Measurements Downstream of a High-Pressure Turbine," *Transactions fo the ASME*, Vol. 120, Oct. 1998, pp. 760-767.
7. Copenhaver, W.W., "Stage Effects on Stalling and recovery of a High-Speed 10-Stage Axial-Flow Compressor," WRDC-TR-90-2054, 1989.
8. Dowell, E.H., Hall, K.C., Thomas, J.P., Florea, R., et al., "Reduced Order Models in Unsteady Aerodynamics," AIAA-99-1261.
9. Drela, M., "XFOIL: An Analysis and Design System for Low Reynolds Number Airfoils," Dept. of Aeronautics and Astronautics, M.I.T, Cambridge, MA.
10. Gander, M.J., MacPherson, W.N., Barton, J.S., Reuben, R.L., et al., "Embedded Micromachine Fiber-Optic Fabry-Perot Pressure Sensors in Aerodynamics Applications", *IEEE Sensors Journal*, Vol. 3, No. 1, Feb. 2003, pp. 102-107.
11. Gracey, W., "Wind-Tunnel Investigation of a Number of Total-Pressure Tubes at High Angles of Attack," NASA TN 3641, May 1956.
12. Hottel, H.C., Kalitinsky, A., "Temperature Measurements in High Velocity Air Streams," ASME 67, 1945.
13. Jackson, D.J., "Aerodynamic Mixing Losses and Discharge Coefficients Due to Film Cooling from a Symmetric Turbine Airfoil in Transonic Flow," M.S. Thesis, Dept. of Mechanical Engineering, University of Utah, Dec. 1998.
14. Kidd, S.R., Barton, J.S., Inci, M.N., Jones, J.D.C., "Unsteady Gas Temperature Measurement Using an Ultra-Short Optical Fibre Fabry-Pérot Interferometer,"*Measurement Science and Technology*, Vol. 5, 1994, pp. 816-822.
15. Kidd, S.R., Barton, J.S., Meredith, P., Jones, J.D.C., et al., "A Fiber Optic Probe for Gas Total Temperature Measurement in Turbomachinery," *Journal of Turbomachinery*, Vol. 117, Oct. 1995, pp. 635-641.
16. Kiel, G., "Total-Head Meter with Small Sensitivity to Yaw," NASA TM 775, Aug. 1935.
17. Kilpatrick, J.M., MacPherson, W.N., Barton, J.S., Jones, J.D.C., et al., "Measurement of Unsteady Gas Temperature with Optical Fibre Fabry-Perot

Microsensors," *Measurement Science and Technology*, Vol. 13, 2002, pp. 706-712.
18. Kupferschmied, P., Köppel, P., Gizzi, W., et al., "Time-Resolved Flow Measurements with Fast-Response Aerodynamic Probes in Turbomachines," *Measurement Science and Technology*, Vol. 11, 2000, pp. 1036-1054.
19. Markowski, S.J. and Moffat, E.M., "Instrumentation for the Development of Aircraft Power Plant Components Involving Fluid Flow," *S.A.E. Quarterly Transactions*, Vol. 2 No. 1, January 1948, pp. 104-116.
20. Moffatt, E.M., "Errors in High Temperature Probes for Gases," ASME 48-A-52, 1948.
21. Moffat, R.J., "Gas Temperature Measurement," *Temperature, Its Measurement and Control in Science and Industry*, Vol. 3, pt. 2, 1962, pp. 553-571.
22. Ng, W.F., Epstein, A.H., "High-Frequency Temperature and Pressure Probe for Unsteady Compressible Flows," *Review of Scientific Instruments*, Vol. 54 No. 12, Dec. 1983, pp. 1678-1683.
23. Rhodes, R., Moeller, T., "Numerical Model of an Aspirated Temperature Probe," AIAA 2011-1202.
24. Rossow, V.J., "Probe Shapes for Streamwise Momentum and Cross-Stream Turbulence Intensity," *Journal of Aircraft*, Vol. 28, no. 11, Nov. 1991, pp. 741-749
25. Scadron, M.D., and Warshawsky, I., "Experimental Determination of Time Constants and Nusselt Numbers for Bare Wire Thermocouples in high Velocity Air Streams and Analytic Approximation of Conduction and Radiation Errors," NACA TN 2599, Jan. 1952.
26. Sieverding, C.H., Arts, T., Dénos, R., Brouckaert, J.F., "Measurement Techniques for Unsteady Flows in Turbomachines," *Experiments in Fluids*, Vol. 28, 2000, pp. 285-321.
27. Simmons,F.S., "Recovery Corrections for Butt-Welded, Straight-Wire Thermocouples in High-Velocity, High-Temperature Gas-Streams," NACA RM E54G22a, Sept. 1954.
28. Society of Automotive Engineers, "Thermoelectric Circuits and the performance of several jet engine thermocouples", SAE Aeronautical Information Rept., A.I.R. 65, 1956.
29. Society of automotive engineers, "Preparation and use of chromel-alumel thermocouples for turbo-jet engines," SAE aeronautical information Rept., A.I.R. 46, 1958.
30. Suryavamshi, N., Lakshminarayana, B., Prato, J., "Aspirating Probe Measurements of the Unsteady Total Temperature Field Downstream of an Embedded Stator in a Multistage Axial Flow Compressor," *Transactions of the ASME*, Vol. 120, January 1998, pp. 156-169.
31. Tommasini, R.M., "A Parametric Study that Analytically Defines the Effect of Reynolds Number on the Temperature Recovery of Total Temperature Sensors in Steady Uniform Flow," PWA-5514, 21 April 1977.

32. Weinstein, L.M., “A Shielded Fine-Wire Probe for Rapid Measurement of Total Temperature in High-Speed Flows,” *Journal of Spacecraft*, Vol. 8 No. 4, Apr. 1971, pp. 425-428.
33. Wennerstrom, A.J., Derose, R.D., Law, C.H., Buzzell, W.A., “Investigation of a 150 ft/sec, Transonic, High-Through-Flow, Single Stage Axial Flow Compressor with Low Hub/Tip Ratio,” AFAPL-TR-76-92, Oct. 1976.
34. Willbanks, C.E., “Recovery Characteristics of a Single-Shielded Self-Aspirating Thermocouple Probe at Low Pressure Levels and Subsonic Speeds,” *Journal of Physics E: Scientific Instruments*, Vol. 6, No. 11, Nov. 1973, pp. 1140-1144.
35. Willcox, K.E., “Reduced-Order Aerodynamic Models for Aeroelastic Control of Turbomachines,” Ph.D Dissertation, Dept. of Aeronautics and Astronautics, M.I.T., Cambridge, MA, Feb. 2000.
36. Winternitz, F.A.L., “Simple Shielded total-Pressure Probes”, *Aircraft Engineering and Aerospace Technology*, Vol. 30 no. 10, Oct. 1958, pp.313 – 317.
37. Xiang, H., Ma, H., Ren, M., Honghui, X., “Investigation of the Effects of Airfoil-probes on the Aerodynamic Performance of an Axial Compressor,” *Chinese Journal of Aeronautics*, Vol. 25, 2012, pp. 517-523